

CROSSROADS IN EARTH AND PLANETARY MATERIALS

Investigation of the kieserite–szomolnokite solid-solution series, $(\text{Mg,Fe})\text{SO}_4 \cdot \text{H}_2\text{O}$, with relevance to Mars: Crystal chemistry, FTIR, and Raman spectroscopy under ambient and martian temperature conditions

DOMINIK TALLA^{1,*} AND MANFRED WILDNER¹

¹Institut für Mineralogie und Kristallographie, Althanstraße 14, 1090 Wien, Austria

ABSTRACT

The investigation of hydrous sulfate deposits and sulfate-cemented soils on the surface of Mars is one of the important topics in the recent scientific endeavor to retrieve detailed knowledge about the planetary water budget and surface weathering processes on our neighbor planet. Orbital visible/near-IR spectra of the surface of Mars indicate kieserite, $\text{MgSO}_4 \cdot \text{H}_2\text{O}$, as a dominant sulfate species at lower latitudes. However, given the Fe-rich composition of the martian surface, it is very probable that its actual composition lies at an intermediate value along the solid-solution series between the kieserite and szomolnokite ($\text{FeSO}_4 \cdot \text{H}_2\text{O}$) end-members. Despite the known existence of significant lattice parameter changes and spectral band position shifts between the two pure end-members, no detailed crystal chemical and spectroscopic investigation along the entire kieserite–szomolnokite solid solution range has been done yet.

The present work proves for the first time the existence of a continuous kieserite–szomolnokite solid-solution series and provides detailed insight into the changes in lattice parameters, structural details, and positions of prominent bands in FTIR ($5200\text{--}400\text{ cm}^{-1}$) and Raman ($4000\text{--}100\text{ cm}^{-1}$) spectra in synthetic samples as the Fe/Mg ratio progresses, at both ambient as well as Mars-relevant lower temperatures. Additionally, an UV-Vis-NIR ($29000\text{--}3500\text{ cm}^{-1}$) crystal field spectrum of szomolnokite is presented to elucidate the influence of Fe^{2+} -related bands on the overtone- and combination mode region.

The kieserite–szomolnokite solid-solution series established in this work shows Vegard-type behavior, i.e., lattice parameters as well as spectral band positions change along linear trends. The detailed knowledge of these trends enables semi-quantitative estimations of the Fe/Mg ratio that can be applied to interpret martian monohydrated sulfates in data from remote sensing missions on a global scale as well as from in situ rover measurements. Given the knowledge of the surface temperature during spectral measurements, the established temperature behavior allows quantitative conclusions concerning the Fe/Mg ratio. Our understanding of the kieserite–szomolnokite solid-solution series will be well applicable to the Mars 2020 and ExoMars 2020 rover missions that will focus on near IR (0.9 to $3.5\text{ }\mu\text{m}$) and, for the first time on Mars, Raman spectroscopy.

Keywords: Kieserite–szomolnokite solid solution, Mars mineralogy, crystal chemistry, FTIR spectroscopy, Raman spectroscopy, UV-Vis-NIR spectroscopy

INTRODUCTION

The surprising discovery of large amounts of sulfate minerals on the surface of Mars dates from the late 1970s when Viking landers carried out the first in situ analyses of martian soils. Using X-ray fluorescence spectroscopy, the presence of diverse Mg- and Ca-dominated sulfate salts was anticipated, in addition to NaCl (Keil et al. 1978; Clark and Van Hart 1981). The sulfates are presumed to originate from acidic weathering of basaltic rock-forming minerals such as olivine and pyroxene, which are believed to contain significant amounts of Fe (Christensen et al. 2004; Schröder et al. 2004; Morrison et al. 2018). Further in situ measurements of the soil composition confirming sulfates took place at Meridiani Planum and Gusev crater using data from the alpha particle X-ray spectrometer (APXS), Mössbauer spectrometer, and the Miniature Thermal Emission Spectrometer (Mini-

TES) on the Opportunity and Spirit rovers (landed in 2004). The terrain at Meridiani Planum consists of bright, layered sediments cemented by various sulfates—interpreted to be predominantly kieserite, $\text{MgSO}_4 \cdot \text{H}_2\text{O}$, and jarosite, perhaps also minor bassanite, thenardite, and some halite (Clark et al. 2005). They extend across vast regions of Meridiani Planum (Christensen et al. 2004; Clark et al. 2005; Glotch et al. 2006) as well as adjacent areas of Terra Meridiani (Arvidson et al. 2005). The formation of the sulfates and the cementation of the sediment by them are believed to have been caused by percolating underground water or sulfate-rich brines with partial contribution from overland flow or body of water (Christensen et al. 2004). However, Knauth et al. (2005) suggest that the observed sedimentary structures could also be ascribed to impact surges from a large nickel-iron meteorite. Papike et al. (2007) note that especially kieserite, via partial Fe-, Ni-, or Co-incorporation, could be an indicator for meteorite impacts as relevant processes in the formation and redistribution of sulfates on Mars.

* E-mail: dominik.talla@univie.ac.at

On a global martian scale, water-equivalent hydrogen (WEH) maps and OMEGA (Observatoire pour la Minéralogie, l'Eau, les Glaces et l'Activité) data indicate variable, low (in comparison with higher latitudes), but still significant amounts of water bound in minerals and buried water ice in the equatorial regions ranging up to 10 wt% (Feldman et al. 2004; Milliken et al. 2007), despite instability of the latter under the prevailing surface conditions. In general, the data suggest that sulfates of varying hydration state, including kieserite, probably represent the dominant water reservoir and also play a key role in the sulfur cycle at lower (<45°) and equatorial martian latitudes (Feldman et al. 2004; Gendrin et al. 2005; Milliken et al. 2007; Mangold et al. 2008; Bishop et al. 2009; Roach et al. 2010; Lichtenberg et al. 2010; Karunatillake et al. 2014; Noel et al. 2015). OMEGA spectra confirmed surficial accumulations of hydrous sulfates (including kieserite) in various regions within Valles Marineris and elsewhere, spatially correlated with layered terrains (Gendrin et al. 2005). High-resolution Compact Reconnaissance Imaging Spectrometer for Mars (CRISM) data offer a more detailed insight into the stratigraphy of such layered sulfate deposits in Juventae Chasma (Bishop et al. 2009; Noel et al. 2015) and West Candor Chasma. In the latter case, Mangold et al. (2008), considering Mars Orbiter Laser Altimeter data (MOLA), found potential indications for kieserite being the primary sulfate cementing the layered terrains, since it is dominant on steeper slopes, while higher sulfate hydrates prevail on the flatter regions where the eroded primary material accumulates and partially rehydrates. Large sulfate deposits with kieserite are known to occur in Ius Chasma (Roach et al. 2010) and Aram Chaos (Lichtenberg et al. 2010), which possibly formed by evaporation of a surface body of water.

Given these finds, as well as the long-term knowledge of the martian soil containing many Fe-rich phases investigated in greater detail by Dyar and Schaefer (2004) and Dyar et al. (2013), it is very probable that the actual composition of martian monohydrated sulfates will represent various intermediate species along the binary join between kieserite and the isotypic Fe end-member szomolnokite, $\text{FeSO}_4 \cdot \text{H}_2\text{O}$, which have partial or complete miscibility. Despite reference data having been obtained from the kieserite and szomolnokite end-members, showing significant shifts of the spectral features and lattice parameters (Chio et al. 2007; Lane 2007; Lane et al. 2015), no detailed investigation of the crystal chemical and spectral characteristics along the entire kieserite–szomolnokite solid-solution series was done so far. However, the structural and crystal chemical evolution along the continuous kieserite–cobaltkieserite solid-solution series, $(\text{Mg},\text{Co})\text{SO}_4 \cdot \text{H}_2\text{O}$, was recently investigated by Bechtold and Wildner (2016), indicating that complete miscibility might also be expected for the $(\text{Mg},\text{Fe})\text{SO}_4 \cdot \text{H}_2\text{O}$ system.

In this paper, we present the results of detailed structural, crystal chemical, FTIR, and Raman spectroscopic investigations on synthetically prepared members along the kieserite–szomolnokite binary solid solution, $\text{Mg}_{1-x}\text{Fe}_x\text{SO}_4 \cdot \text{H}_2\text{O}$, at ambient and lower temperatures, as relevant for Mars surface conditions, complemented by UV-Vis-NIR crystal field spectra of Fe^{2+} in szomolnokite. The presented data may prove invaluable in further refining the chemical composition of martian monohydrated sulfates based on available remote sensing data in the mid-infrared

range, as well as be a fundamental data set for interpreting future in situ data from forthcoming Mars rovers, in particular data from the SuperCam (Wiens et al. 2017a, 2017b) and Scanning Habitable Environments with Raman & Luminescence for Organics & Chemicals (SHERLOC; Beegle et al. 2014) instruments onboard the Mars 2020 rover (NASA) and the Raman Laser Spectrometer (RLS; Rull et al. 2017; Rull 2018) and Infrared Spectrometer for ExoMars (ISEM; Dobrolenskiy et al. 2017) instruments onboard the ExoMars 2020 rover (ESA).

EXPERIMENTAL METHODS

Sample preparation

The hydrothermal technique was used to synthesize crystalline material with a pre-adjusted Mg/Fe ratio along the kieserite–szomolnokite solid solution using polytetrafluoroethylene-lined stainless steel autoclaves with an inner volume of ~55 cm³. Each autoclave was filled with $\text{MgSO}_4 \cdot 7\text{H}_2\text{O}$ and $\text{FeSO}_4 \cdot 7\text{H}_2\text{O}$ amounting to 6 g in total, to obtain a specific Mg/Fe ratio in the resulting crystals; H_2SO_4 ($w = 0.73$) was added as a solvent. All reagents were of analytical grade. Initial problems regarding partial oxidation of Fe^{2+} to Fe^{3+} , leading to the formation of unwanted phases as well (e.g., rhomboclase and other Fe^{3+} or mixed $\text{Fe}^{2+}/\text{Fe}^{3+}$ sulfates) required the use of a redox buffer.

In the first series of buffered synthesis runs, a foil of metallic iron (dimensions $3 \times 10 \times 1$ mm) was used, with the addition of 25 cm³ H_2SO_4 ($w = 0.73$). Despite the positive effect of the foil leading to $(\text{Mg},\text{Fe})\text{SO}_4 \cdot \text{H}_2\text{O}$ forming as practically the sole product, a part of the metal dissolved in the acid, causing the crystals to be significantly enriched in Fe relative to the pre-set Mg/Fe ratio. Hence, these synthesis attempts were stopped after the Mg-dominant batch runs in favor of the preferred use of 5 mL H_2SO_3 ($w = 0.06$) as the redox buffer instead, added along with 20 cm³ H_2SO_4 ($w = 0.73$) as solvent, in all subsequent experiments for the full range of Mg/Fe ratios.

The filled hydrothermal autoclaves were placed into a programmable furnace and heated at a rate of 50 °C/h to 210 °C. Following a holding time of 24 h to ensure complete dissolution of the contents, a cooling rate of 3 °C/h down to room temperature was applied. After decantation of the acid and mechanical removal of the solids from the reaction vessel, the product was washed twice with distilled H_2O , taking advantage of the relatively slow dissolution rate of the sulfate monohydrates. Following a twofold washing process using 98% ethanol to remove H_2O from the previous step, the product was dried in an oven at 65 °C overnight. The resulting colorless to light beige material was stored in airtight vials. Microscopic inspection showed the batches to consist predominantly of fine crystals (10–50 µm) and crystal aggregates, with sporadic larger individuals (up to ~300 µm), the latter revealing dipyrarnidal habit and pronounced sectoral or polysynthetic twinning.

To our surprise, the crystals, as long as they are free of residues of the parent solution, are stable in air over long time scales (years to decades; even original crystals of $\text{FeSO}_4 \cdot \text{H}_2\text{O}$ from the syntheses of Wildner and Giester 1991 are still preserved), with only close-to-end-member $\text{MgSO}_4 \cdot \text{H}_2\text{O}$ slowly transforming to higher hydrates.

Chemical analyses and powder X-ray diffraction

Wet chemical analyses were done on a part of each sample batch at the Masaryk University in Brno, Czech Republic. An amount of ~0.5 g of ground sample material was dissolved in boiling HNO_3 ($w = 0.65$). Contents of Mg and Fe were both determined by atomic absorption analysis (instrument Solaar M5 and TJA solutions, measurement time 4 s per element) with an analytical error of 0.005 wt% for Mg and 0.002 wt% for Fe.

A further part of each sample batch was examined using powder X-ray diffraction. The material was pressed onto an Si-holder and measured on a Philips PW 3710 diffractometer (measuring interval 5–120 °2θ in 0.2° increments, measuring time of 15 s per step). The Bruker EVA 2013 software with its database was used for the preliminary phase identification, then Rietveld refinements using the Bruker program TOPAS3 were performed to confirm expected lattice parameter shifts and the mono-phase character of the solid solutions.

Single-crystal X-ray diffraction

Hand-picked single crystals suitable for X-ray diffraction measurements were obtained by crushing crystal aggregates and choosing fragments with homogeneous extinction under crossed polars. The crystal structures of 10 representatives of the

Mg_{1-x}Fe_xSO₄·H₂O solid-solution series, including the szomolnokite end-member, were determined from single-crystal X-ray diffraction data, measured at 295 K with graphite-monochromatized MoK α radiation on a Nonius Kappa CCD diffractometer equipped with a 0.3 mm monocrapillary X-ray optics collimator. Complete Ewald spheres up to $2\theta = 80^\circ$ were each collected in several sets of φ - and ω -scans with 2° rotation per CCD frame, at a crystal to detector distance of 30 mm. The integration and correction of the intensity data, including an absorption correction by multi-frame scaling and the refinement of lattice parameters, were done with the program DENZO-SMN (Nonius 1998).

Temperature-dependent X-ray data collections of the kieserite and szomolnokite end-members were performed between +40 and -160 °C in steps of 40 K on a Bruker ApexII diffractometer equipped with a CCD area detector and an Incoatec Microfocus Source I μ S (30 W, multilayer mirror, MoK α), in a dry stream of nitrogen (Cryostream 800, Oxford Cryosystems). Several sets of φ - and ω -scans with 2° scan width were measured at a crystal-detector distance of 40 mm up to 80° 2θ full sphere. Absorption was corrected by evaluation of multi-scans. For the sake of data consistency, the lattice parameters extracted from the ApexII temperature-dependent measurements were corrected in such a way that their interpolated values at 20 °C match those obtained from the Nonius Kappa CCD room-temperature measurements of the very same two end-member crystals.

All structure refinements were performed on F^2 with SHELXL-97 (Sheldrick 2008) in the “traditional” non-reduced kieserite cell setting. Scattering curves for neutral atoms were used. The Mg/Fe ratios of the particular single crystals studied were extracted as a refined variable in the respective structure refinement runs.

CIF data for room-temperature structures included in Tables 1 and Supplemental¹ Table S1 (plus CIF of end-member kieserite from Bechtold and Wildner 2016) and of temperature-dependent structures included in Table 3 and Supplemental¹ Table S2 have been deposited.

IR spectroscopy

A part of each sample batch in powdered form and beforehand characterized by wet-chemical and powder X-ray diffraction analyses (see above) was used to conduct FTIR measurements in transmission, Attenuated Total Reflectance (ATR) and Diffuse Reflectance Infrared Fourier Transform (DRIFT) modes by means of the Bruker Tensor 27 FTIR spectrometer (Globar light source, KBr beam splitter, DTGS detector). For transmission measurements, the sample material was diluted in KBr at a weight ratio of 1:300 and pressed into pellets in a vacuum press. ATR measurements were done using the mountable Bruker ATR unit by pressing the sample powder against the diamond surface. For DRIFT measurements, the powder was pressed into the sample holder of a Perkin-Elmer DRIFT unit. Finely ground

MgO was used as the reflectivity standard for the background measurements. All reflectance data were corrected via the Kubelka-Munk equation implemented in the Bruker OPUS software. The full wavenumber range (7000–400 cm⁻¹) was investigated in all analytical modes with a spectral resolution of 4 cm⁻¹ (2 cm⁻¹ spectral sampling). Each spectrum was averaged from 50 scans to reduce noise. For the DRIFT analyses, each sample was measured in a pure state, as well as diluted with KBr in a ratio of 1:20, to enhance the absorption contribution to the resulting spectrum.

Low-temperature FTIR transmission measurements were done using a Linkam FTIR600 cooling stage equipped with KBr windows. KBr micropellets (2 mm diameter, sample dilution ratio 1:300) with the material pressed into the aperture of a steel gasket were used for these investigations. The metal gasket along with the small sample volume ensured easy handling and swift thermal conductivity between the Ag-block of the cooling stage and the sample. Measurements were done in 40 K intervals ranging from 313 K (40 °C) down to 113 K (-160 °C). Some additional measurements at 93 K (-180 °C) were done occasionally.

Raman spectroscopy

Raman spectra were measured on a Horiba Jobin Yvon LabRam-HR spectrometer, equipped with an Olympus BX41 optical microscope. A diffraction grating with 1800 grooves/mm and the 633 nm laser were used. The system is equipped with a Si-based, Peltier-cooled charge-coupled device (CCD) detector. A 100 \times objective (NA = 0.55) was selected for all room-temperature measurements. The wavenumber accuracy was better than 0.5 cm⁻¹, and the spectral resolution was determined to be ~ 0.3 cm⁻¹. The room-temperature Raman spectra were acquired between 100–4000 cm⁻¹ shift, using multi-window scans with a counting time of 50 s per window and repeating every scan twice to eliminate spikes.

Low-temperature Raman measurements were conducted using the Linkam FTIR 600 cooling stage. Single crystals were placed on the Ag-block covered with a thermal conducting fluid. The use of single crystals instead of powdered material was essential, despite the inherent problems due to varying and unknown crystal orientation, as only single-crystal material allowed short-enough measuring times to prevent excessive ice buildup on the sample surface. The bulky stage necessitated the use of a long-distance 50 \times objective, with otherwise the same setup of the Raman instrument. The spectra were acquired in two separate spectral regions, i.e., 100–1600 and 2800–4000 cm⁻¹ shift, with 5 s measuring time per window. Most acquisition temperatures match those of the FTIR low-temperature measurements to allow for direct comparison.

Band positions for both FTIR and Raman spectra were obtained by fitting the spectra in the program Peakfit (v.4.0). A Voigt-shaped band profile (i.e., a convolu-

TABLE 1. Crystal data and details of room-temperature X-ray data collections and structure refinements for selected representatives of the Mg_{1-x}Fe_x(SO₄)·H₂O solid-solution series

Mg _{1-x} Fe _x (SO ₄)·H ₂ O	Mg _{1.00} Fe _{0.00}	Mg _{0.86} Fe _{0.14}	Mg _{0.55} Fe _{0.45}	Mg _{0.25} Fe _{0.75}	Mg _{0.00} Fe _{1.00}
x_{Fe}	0.0	0.138(2)	0.450(2)	0.752(3)	1.0
<i>a</i> (Å)	6.910(1)	6.938(1)	6.989(1)	7.042(1)	7.086(1)
<i>b</i> (Å)	7.634(2)	7.621(1)	7.601(1)	7.579(2)	7.555(1)
<i>c</i> (Å)	7.643(2)	7.663(1)	7.710(1)	7.753(2)	7.780(1)
β (°)	118.00(1)	118.14(1)	118.30(1)	118.49(1)	118.61(1)
<i>V</i> (Å ³)	356.00(14)	357.32(8)	360.63(8)	363.65(14)	365.63(8)
μ (mm ⁻¹)	0.97	1.48	2.61	3.70	4.58
<i>D</i> _{calc} (g/cm ³)	2.582	2.653	2.810	2.961	3.087
Exposure time (s)/frame	140	150	25	70	40
CCD frames processed	508	526	503	514	511
Frame scale factor _{S_{max}, min}	1.11, 0.89	1.12, 0.91	1.16, 0.81	1.17, 0.76	1.09, 0.77
Total number of intensity data	12919	14115	13849	14055	12661
Total number of reflections	8865	8935	8613	8615	8875
Intensity data for unit cell	5101	7219	7420	7418	5362
Number of <i>hkl</i> values	3995	4178	4203	4211	4255
Unique <i>hkl</i> values	1089	1100	1110	1126	1133
<i>R</i> _i (%)	3.20	2.77	2.37	3.09	2.65
<i>F</i> _o > 4 σ (<i>F</i> _o)	937	985	1026	1027	1111
Variables	39	42	42	42	40
wR2 [for all <i>F</i> _o ²] (%)	6.17	5.75	5.72	5.98	4.12
weighting parameters <i>a</i> , <i>b</i> ^a	0.028, 0.20	0.027, 0.27	0.028, 0.20	0.030, 0.32	0.018, 0.27
R1 [for <i>F</i> _o > 4 σ (<i>F</i> _o)] (%)	2.27	2.23	2.20	2.39	1.56
R1 [for all <i>F</i> _o ²] (%)	2.94	2.73	2.53	2.82	1.60
Goodness of fit	1.109	1.062	1.151	1.073	1.065
Extinction coefficient	0	0.004(2)	0.009(2)	0.009(2)	0.260(5)
$\Delta\rho_{max, min}$ (e ⁻ Å ⁻³)	0.47, -0.51	0.59, -0.43	0.95, -0.45	1.02, -0.49	0.77, -0.62

Notes: Common data: monoclinic, space group C2/c (no. 15), *Z* = 4. Data for the kieserite end-member are taken from Bechtold and Wildner (2016).

^a $w = 1/[\sigma^2(F_o^2) + (a \times P)^2 + b \times P]$; $P = \{[\max(0, F_o)] + 2F_o^2\}/3$.

tion of Gaussian and Lorentzian shapes) was used in both cases. Initial estimates of the number of bands and their distribution in IR and Raman spectra were based on the investigations on kieserite by previous authors (Stoilova and Lutz 1998; Lane 2007; Lane et al. 2015 for FTIR spectra; and Chio et al. 2007 and citations therein for Raman spectra).

UV-Vis-NIR spectroscopy and crystal field calculations

An unpolarized optical absorption spectrum of a single crystal of $\text{FeSO}_4 \cdot \text{H}_2\text{O}$ was measured at room temperature in the spectral range $30\,000\text{--}3500\text{ cm}^{-1}$ on a mirror-optics microscope IRscope-II, attached to a Bruker IFS66v/S FTIR spectrometer. Appropriate combinations of light sources (Xe- or W-lamp, Globar), beam splitters (quartz, KBr) and detectors (GaP-, Si-, Ge-diodes, MCT) were used to cover the spectral range. The final spectrum is combined from four partial spectra (range in cm^{-1} /spectral resolution in cm^{-1} /averaged scans: UV: $30\,000\text{--}19\,380/40/1024$; Vis: $19\,380\text{--}9700/20/1024$; NIR: $9700\text{--}5260/10/768$; IR: $5260\text{--}3000/4/512$), which were aligned in absorbance for perfect match, if necessary, and then converted to the linear absorption coefficient α .

Crystal field (CF) calculations were performed in the framework of the semi-empirical Superposition Model (SM) of crystal fields using the HCFLDN2 module of the computer program package by Y.Y. Yeung (Chang et al. 1994). Due to the small number of observed crystal field levels, the power-law exponents (t_i) were fixed at their respective ideal electrostatic values, i.e., $t_4 = 5$ and $t_2 = 3$, and the Racah parameters were constrained to the ratio $Racah\ C/B = 4.3$ given in Figgis and Hitchman (2000). The reference metal–ligand distance R_0 was set to 2.13 \AA , the mean $\langle\text{Fe-O}\rangle$ bond length in szomolnokite. For further details concerning the calculation procedures, the reader is referred to similar cases in Wildner et al. (2013) and respective references therein.

RESULTS

Sample chemistry and phase purity

The wet chemical analyses ensured precise knowledge of the actual Mg/Fe ratio in the bulk synthesized products in their respective final state, i.e., after the purification process described in the experimental section. In addition, they revealed systematic differences between the pre-adjusted and the actual Mg/Fe ratio in the product. The redox buffer greatly influences the extent of discrepancy between theoretical $x_{\text{Fe}(\text{preset})}$ and experimental $x_{\text{Fe}(\text{sample})}$ values. Whereas the crystals are usually clearly enriched in Fe when using the metallic Fe-foil as redox buffer, preferential incorporation of Fe into the monohydrated sulfate is of a much lesser extent with the H_2SO_3 buffer in use. For the spectroscopic measurements, only batches with $|x_{\text{Fe}(\text{sample})} - x_{\text{Fe}(\text{preset})}| \leq 0.06$ as listed in Table 2 and shown in Figure 1 were used.

Powder X-ray diffraction measurements and Rietveld refinements revealed the various batches to consist nearly exclusively of kieserite-type $(\text{Mg,Fe})\text{SO}_4 \cdot \text{H}_2\text{O}$ with occasional traces of hexahydrite or rhomboclase. The patterns showed no signs of Bragg peak splitting or suspicious broadening, thus confirming compositional homogeneity and the mono-phase character of the obtained monohydrate sulfate solid solutions.

As noted already above, the Mg/Fe ratios of the crystals hand-picked for single-crystal X-ray diffraction studies were extracted as a refined variable in the structure refinements.

Crystal structures

The present single-crystal X-ray measurements and structure refinements along the kieserite–szomolnokite solid-solution series, $\text{Mg}_{1-x}\text{Fe}_x\text{SO}_4 \cdot \text{H}_2\text{O}$, gave no indications of octahedral Mg/Fe cation ordering, domain formation or related effects. Crystal data, details of the data collections and structure refinements of four selected representatives, including szomolnokite are listed in Table 1, respective final atomic coordinates and displacement parameters

TABLE 2. Composition of the spectroscopically studied samples as determined by wet chemical analyses

Sample ID	Mg (wt%)	Fe (wt%)	$x_{\text{Fe}(\text{sample})}$	$x_{\text{Fe}(\text{preset})}$	$x_{\text{Fe}(\text{sample})} - x_{\text{Fe}(\text{preset})}$
Fe10c	15.77	3.73	0.093	0.100	−0.006
Fe15c	13.84	6.54	0.170	0.150	0.020
Fe20c	13.05	7.53	0.200	0.200	0.000
Fe30c	11.87	9.68	0.261	0.300	−0.038
Fe40c	9.85	12.78	0.360	0.400	−0.039
Fe55a	15.81	3.89	0.096	0.050	0.046
Fe105a	14.21	5.42	0.142	0.100	0.042
Fe155a	12.77	7.63	0.206	0.150	0.056
Fe255a	11.05	10.25	0.287	0.250	0.037
Fe455a	7.68	15.84	0.473	0.450	0.023
Fe655a	4.67	20.78	0.659	0.650	0.009
Fe855a	2.36	23.04	0.868	0.850	0.018
Fe05b	16.76	0.05	0.000	0.000	0.000
Fe20Sa	11.87	8.81	0.244	0.200	0.044
Fe30Sa	9.85	12.22	0.350	0.300	0.050
Fe355a	8.82	14.17	0.411	0.350	0.061
Fe40Sa	8.10	14.36	0.435	0.400	0.035
Fe50Sa	6.41	17.99	0.549	0.500	0.049
Fe60Sa	5.14	19.87	0.627	0.600	0.027
Fe70Sa	3.85	22.03	0.713	0.700	0.013
Fe75Sa	3.28	22.65	0.750	0.750	0.000
Fe80Sa	2.36	23.04	0.809	0.800	0.009
Fe90Sa	0.92	24.71	0.920	0.900	0.020
Fe95Sa	0.69	27.19	0.945	0.950	−0.004
Fe100Sa	0.01	27.5	0.999	1.000	0.000
Fe55c	15.89	3.64	0.090	0.050	0.040
Fe80Sc	3.34	22.93	0.749	0.800	−0.050
Fe85Sc	2.49	23.96	0.807	0.850	−0.042
Fe05c	17.59	0	0	0	0

Notes: The analytical error is 0.005 wt% for Mg and 0.002 wt% for Fe. Deviations of the actual sample Fe content $x_{\text{Fe}(\text{sample})}$ from the preset Mg/Fe ratio in the batch $x_{\text{Fe}(\text{preset})}$ are also given. The Mg/Fe ratios of individual hand-picked crystals for single-crystal X-ray diffraction studies were extracted as a variable parameter in the respective structure refinement runs.

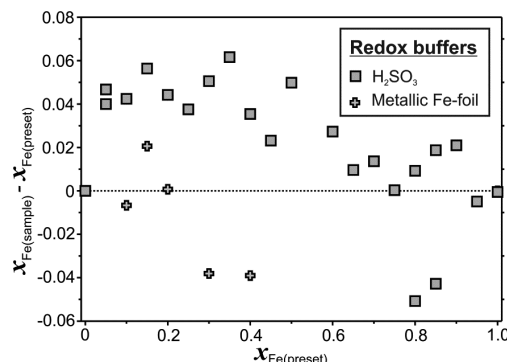


FIGURE 1. Deviations between actual Fe content of the $\text{Mg}_{1-x}\text{Fe}_x(\text{SO}_4) \cdot \text{H}_2\text{O}$ solid solution samples $x_{\text{Fe}(\text{sample})}$ as determined by the wet chemical analyses and the pre-adjusted Mg/Fe ratio in the hydrothermal batch $x_{\text{Fe}(\text{preset})}$. Errors are equal or smaller than the symbol size. Note that batches exceeding the shown range of deviation (i.e., mainly Mg-dominant batch runs with metallic Fe-foil as redox buffer yielding significantly Fe-enriched samples) were not used for the spectroscopic measurements.

in Supplemental¹ Table S1. Corresponding temperature-dependent data of the end-members kieserite and szomolnokite are compiled for two selected temperatures in Table 3 and Supplemental¹ Table S2. Important crystal chemical data at ambient and temperature-dependent conditions are given in Tables 4 and 5, respectively. Details for the kieserite end-member at room temperature were recently reported by Bechtold and Wildner (2016) in their structural study of the kieserite–cobaltkieserite solid-solution series,

TABLE 3. Crystal data and details of selected temperature-dependent X-ray data collections and structure refinements for kieserite and szomolnokite endmembers, Mg/Fe(SO₄)·H₂O

Mg/Fe(SO ₄)·H ₂ O	Mg _{1.00}	Mg _{1.00}	Fe _{1.00}	Fe _{1.00}
T (°C)	–80	–160	–80	–160
a (Å) ^a	6.882(1)	6.865(1)	7.058(1)	7.040(1)
b (Å) ^a	7.653(1)	7.668(1)	7.566(1)	7.576(1)
c (Å) ^a	7.617(1)	7.606(1)	7.758(1)	7.745(1)
β (°) ^a	117.88(1)	117.79(1)	118.45(1)	118.37(1)
V (Å ³)	354.60(9)	354.18(9)	364.23(9)	363.48(9)
μ (mm ^{–1})	0.97	0.97	4.60	4.61
D _{calc} (g/cm ³)	2.592	2.595	3.099	3.105
CCD frames processed	748	748	766	766
Transmission factor _{S_{max},min}	0.69, 0.75	0.69, 0.75	0.57, 0.75	0.58, 0.75
Total number of reflections	10428	10307	10851	10783
Intensity data for unit cell	6649	7061	8498	8607
Unique hkl values	1098	1097	1131	1128
R _i (%)	1.96	1.84	2.60	2.13
F _o > 4σ(F _o)	1047	1054	1112	1118
wR ₂ [for all F _o] (%)	4.48	4.26	3.38	3.22
weighting parameters a, b ^b	0.020, 0.18	0.018, 0.21	0.015, 0.20	0.013, 0.24
R1 [for F _o > 4σ(F _o)] (%)	1.56	1.48	1.28	1.27
R1 [for all F _o] (%)	1.67	1.56	1.31	1.29
Goodness of fit	1.202	1.207	1.168	1.193
Extinction coefficient	0.004(2)	0.006(2)	0.033(1)	0.042(1)
Δρ _{max,min} (e [–] Å ^{–3})	0.49, –0.37	0.46, –0.40	0.49, –0.52	0.68, –0.44

Note: Common data: monoclinic, space group C2/c (no. 15), Z = 4; Exposure time/frame 20 s; 40 variables. Respective room-temperature data for kieserite (Bechtold and Wildner 2016) and szomolnokite are given in Table 1.

^a Lattice parameters are corrected to comply with data from Nonius Kappa CCD room temperature measurements of the same two crystals (see Experimental section).

^b $w = 1/[\sigma^2(F_o) + (a\sigma P)^2 + b\sigma P]$; $P = \{[\max \text{ of } (0 \text{ or } F_o^2)] + 2F_o^2\}/3$.

and are included in Tables 1 and 4 for comparison.

The kieserite structure type is built from kinked chains of O3(=H₂O)-corner-sharing MgO₄(H₂O)₂ octahedra, elongated along their O3–O3 axis, and nearly regular SO₄ tetrahedra, intra-linking adjacent octahedra within the chains by common O2 corners. These octahedral-tetrahedral chains are aligned parallel to the *c* axis and linked to a framework structure by sharing the remaining polyhedral O1 corners as well as by moderately strong O3···O2 hydrogen bonds.

The structural behavior of the Mg_{1–x}Fe_xSO₄·H₂O kieserite–szomolnokite solid-solution series is illustrated in Figures 2–5. It is evident that complete miscibility exists and that the series shows Vegard-type behavior, with all lattice parameters (Fig. 2) changing in a linear way across the entire composition. The cell volume *V* (+10 Å³), angle β (+0.6°), and the lattice parameters *a* and *c* (+0.18 and 0.14 Å) increase with Fe uptake, only the *b* axis (–0.08 Å) shows an opposite trend. The clear increase of individual and average Me–O bond lengths and of the octahedral volume (Figs. 3a and 4a) comply with the larger ionic radius of Fe²⁺ compared to Mg. The comparatively moderate increase of the Me–O2 bond can be partly related with the shortening of the *b* axis, since Me–O1, –O2, and –O3 bonds have their major vector components parallel to the crystallographic *a*, *b*, and *c* axis, respectively. With Fe uptake, the octahedral distortion also increases for bond lengths as well as bond angles (Figs. 3a and 3b, Table 4), and the octahedral shape changes from a clear [4+2] coordination in kieserite toward a [2+2+2]-type coordination in szomolnokite. In addition, the tetrahedral SO₄ group slightly expands with increasing Fe content (Figs. 3c and 4a), but the bond length and angular changes (Fig. 3d) hardly exceed a 3σ limit. The medium-strength hydrogen bond O3–H···O2 lengthens only

TABLE 4. Survey of crystal chemical data at room temperature for selected representatives of the Mg_{1–x}Fe_x(SO₄)·H₂O solid-solution series: bond lengths (Å) and angles (°), polyhedral volumes (Å³), bond strengths (without H atoms; calculated according to Brese and O'Keeffe 1991), and polyhedral distortion parameters (Brown and Shannon 1973; Robinson et al. 1971; Griffen and Ribbe 1979)

Mg _{1–x} Fe _x (SO ₄)·H ₂ O	Mg _{1.00} Fe _{0.00}	Mg _{0.86} Fe _{0.14}	Mg _{0.55} Fe _{0.45}	Mg _{0.25} Fe _{0.75}	Mg _{0.00} Fe _{1.00}
X _{Fe}	0.0	0.138(2)	0.450(2)	0.752(3)	1.0
Me–O1 (2×)	2.0216(7)	2.0327(7)	2.0585(7)	2.0854(8)	2.1079(6)
Me–O2 (2×)	2.0414(7)	2.0436(6)	2.0493(6)	2.0545(8)	2.0567(6)
Me–O3 (2×)	2.1714(6)	2.1800(5)	2.1996(5)	2.2183(7)	2.2314(4)
<Me–O>	2.0782	2.0854	2.1025	2.1194	2.1320
Δ _{oct} × 10 ³	1.023	1.033	1.070	1.124	1.183
Σv.u. (Me)	2.15	2.14	2.12	2.10	2.09
O1–Me–O2 (2×) ^a	85.91(3)	85.82(3)	85.59(3)	85.36(3)	85.08(3)
O1–Me–O3 (2×) ^a	88.50(2)	88.19(2)	87.59(2)	86.96(2)	86.48(2)
O2–Me–O3 (2×) ^a	87.20(3)	87.28(3)	87.49(3)	87.67(4)	87.84(3)
σ _{oct} ²	9.75	10.24	11.48	13.16	15.00
V _{oct}	11.901(10)	12.024(8)	12.314(8)	12.604(11)	12.820(8)
S–O1 (2×)	1.4639(7)	1.4629(6)	1.4636(6)	1.4638(8)	1.4638(6)
S–O2 (2×)	1.4817(7)	1.4818(6)	1.4833(6)	1.4849(8)	1.4868(5)
<S–O>	1.4728	1.4724	1.4735	1.4743	1.4753
BLDP × 10 ³	6.98	7.41	7.72	8.28	9.00
Σv.u. (S)	6.02	6.03	6.01	6.00	5.98
O1–S–O1'	109.94(6)	109.98(6)	110.11(6)	110.20(8)	110.31(6)
O1–S–O2 (2×)	108.59(4)	108.59(4)	108.73(4)	108.85(4)	108.79(3)
O1–S–O2' (2×)	110.41(4)	110.42(4)	110.24(4)	110.11(5)	110.15(4)
O2–S–O2'	108.89(6)	108.84(5)	108.76(5)	108.70(7)	108.62(5)
σ _{tetr} ²	0.77	0.80	0.64	0.54	0.66
V _{tetr}	1.639(2)	1.638(2)	1.641(2)	1.644(3)	1.648(2)
Me–O1–S	140.38(4)	139.93(4)	138.77(4)	137.58(5)	136.70(4)
Me–O2–S	134.31(4)	134.28(4)	134.06(4)	133.78(5)	133.41(3)
Me–O3–Me	123.27(5)	123.01(4)	122.40(4)	121.80(5)	121.31(4)
Σv.u. (O1)	1.95	1.95	1.93	1.92	1.91
Σv.u. (O2)	1.86	1.86	1.86	1.87	1.87
Σv.u. (O3)	0.55	0.54	0.53	0.53	0.52
O3···O2	2.7449(8)	2.7478(8)	2.7507(8)	2.7541(9)	2.7565(7)
O3–H	0.81(2)	0.76(2)	0.76(2)	0.82(2)	0.82(2)
O2···H	2.01(2)	2.04(2)	2.06(2)	2.01(2)	2.04(2)
O3–H···O2	151(2)	155(2)	150(2)	151(2)	145(2)

Note: Data for the kieserite end-member are taken from Bechtold and Wildner (2016).

^a Plus corresponding obtuse angles.

slightly (Fig. 4c), despite having its main component parallel to the strongly increasing *a* axis.

The prominent changes within the MeO₆ octahedron along the Mg_{1–x}Fe_xSO₄·H₂O solid solution are accompanied by mutual compensating polyhedral rotations and tiltings, evidenced by a significant decrease of the Me–O–S and Me–O3–Me angles shown in Figure 4b. Hence, the tilting within the octahedral chain increases and the rigid SO₄ tetrahedron rotates by up to 2.3° (O1–O1' edge; O2–O2' edge: 2.0°) around its twofold axis (Fig. 5); combined with the strong change of the octahedral O1–Me–O3 angle this leads to a mutual shift of the polyhedral chains along the *c* axis, resulting in the increase of the cell angle β and especially of the *a* axis.

When the temperature is reduced, some structural properties of the kieserite and szomolnokite end-members seem to deviate more or less from a linear response. As expected, the cell volumes decrease, as well as β, *a*, and *c*, but the *b* axis lengthens for both compounds (Fig. 6). Also the mean Me–O bond lengths (Fig. 7a) and octahedral volumes (Fig. 7c) decrease, mainly by reducing the longest Me–O3 bond; the only other Me–O change larger than 3σ across the whole temperature range is a further slight shortening of shortest Fe–O2 bond; thus, for the FeO₆ octahedron the tendency toward a [2+2+2] coordination still increases. Most acute octahedral bond angles marginally

TABLE 5. Survey of selected temperature-dependent crystal chemical data for kieserite and szomolnokite, $\text{Mg}/\text{Fe}(\text{SO}_4) \cdot \text{H}_2\text{O}$: Bond lengths (\AA) and angles ($^\circ$), polyhedral volumes (\AA^3), bond strengths (without H atoms; calculated according to Brese and O'Keeffe 1991), and polyhedral distortion parameters (Brown and Shannon 1973; Robinson et al. 1971; Griffen and Ribbe 1979)

$\text{Mg}/\text{Fe}(\text{SO}_4) \cdot \text{H}_2\text{O}$	$\text{Mg}_{1.00}$	$\text{Mg}_{1.00}$	$\text{Fe}_{1.00}$	$\text{Fe}_{1.00}$
T ($^\circ\text{C}$)	-80	-160	-80	-160
Me-O1 (2x)	2.0222(5)	2.0222(5)	2.1093(6)	2.1088(5)
Me-O2 (2x)	2.0407(5)	2.0410(5)	2.0551(5)	2.0546(5)
Me-O3 (2x)	2.1640(4)	2.1607(4)	2.2252(4)	2.2217(4)
<Me-O>	2.0756	2.0746	2.1299	2.1284
$\Delta_{\text{oct}} \times 10^3$	0.919	0.874	1.110	1.070
Σ v.u. (Me)	2.16	2.17	2.10	2.10
O1-Me-O2 (2x) ^a	85.97(2)	86.03(2)	85.05(2)	85.04(2)
O1-Me-O3 (2x) ^a	88.51(2)	88.56(1)	86.49(2)	86.54(2)
O2-Me-O3 (2x) ^a	87.23(2)	87.27(2)	87.95(2)	88.01(2)
σ_{oct}^2	9.50	9.20	14.92	14.74
V_{oct}	11.861(6)	11.845(6)	12.783(7)	12.758(6)
S-O1 (2x)	1.4640(5)	1.4647(5)	1.4652(5)	1.4657(5)
S-O2 (2x)	1.4837(5)	1.4849(4)	1.4887(5)	1.4901(5)
<S-O>	1.4739	1.4748	1.4770	1.4779
BLDP $\times 10^3$	7.72	7.91	9.19	9.53
Σ v.u. (S)	6.00	5.99	5.96	5.94
O1-S-O1'	110.01(4)	110.12(4)	110.47(4)	110.59(4)
O1-S-O2 (2x)	108.61(3)	108.63(2)	108.86(3)	108.85(3)
O1-S-O2' (2x)	110.33(3)	110.30(3)	110.06(3)	110.05(3)
O2-S-O2'	108.94(4)	108.85(4)	108.52(4)	108.42(4)
σ_{tet}^2	0.71	0.72	0.69	0.76
V_{tet}	1.643(1)	1.646(1)	1.653(1)	1.656(1)
Me-O1-S	140.00(3)	139.84(3)	136.22(3)	136.04(3)
Me-O2-S	133.63(3)	133.32(3)	132.79(3)	132.45(3)
Me-O3-Me	123.28(3)	123.28(3)	121.28(3)	121.27(3)
Σ v.u. (O1)	1.95	1.95	1.96	1.95
Σ v.u. (O2)	1.86	1.85	1.80	1.80
Σ v.u. (O3)	0.56	0.57	0.53	0.54
O3...O2	2.7292(6)	2.7216(5)	2.7409(6)	2.7316(6)
O3-H	0.81(1)	0.82(1)	0.87(2)	0.85(2)
O2...H	1.98(1)	1.96(1)	1.97(2)	1.95(2)
O3-H...O2	154(1)	156(1)	149(2)	152(1)

Note: Respective room-temperature data for kieserite (Bechtold and Wildner 2016) and szomolnokite are given in Table 4.

^a Plus corresponding obtuse angles.

increase (Fig. 7b), thus slightly reducing bond angle distortion at lower temperatures. If S–O bond lengths are not corrected for thermal motion, the apparent increase in S–O bond lengths and tetrahedral volume upon cooling (Figs. 7c and 7d) has to be assigned as the respective artifact. Applying a “simple rigid bond” correction according to Downs et al. (1992) results (apart from a generally inherent distance increase) in a practically constant <S–O> bond length in kieserite and a marginally decreasing one ($\Delta_{\text{S-O}} = -0.0014 \text{ \AA}$) in szomolnokite upon cooling along the full temperature range. The tetrahedral angles show divergent trends with temperature reduction (with maximal changes of 0.3°), i.e., tending to lower distortion in kieserite compared to higher distortion in szomolnokite. The O3–H...O2 hydrogen bond length consistently shortens in both compounds by $\sim 0.028 \text{ \AA}$ within the investigated 200 K range (Fig. 8a). Also corresponding polyhedral-linking angles show parallel behavior in kieserite and szomolnokite (Fig. 8b): the octahedral chain angle Me–O3–Me remains constant, but Me–O–S angles become smaller by 1.1° (O2) and -0.7° (O1). The resulting rotation of the SO_4 tetrahedron upon cooling has the same sense as found for increasing x_{Fe} in the solid solution (compare Fig. 5); between room temperature and -160°C it amounts to roughly 1.1° for both O1–O1' and O2–O2' tetrahedral edges in both end-members.

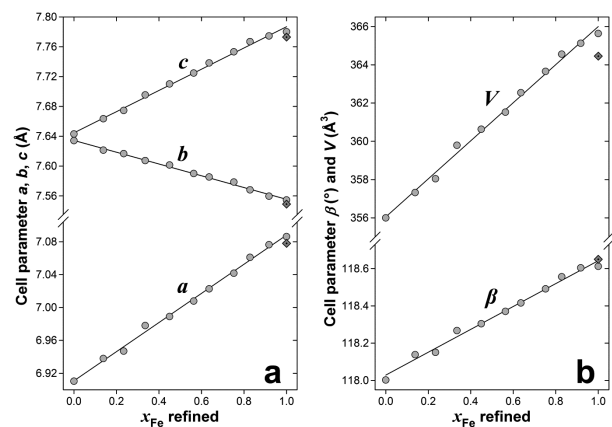


FIGURE 2. Variation of the lattice parameters (a) a , b , c , and (b) β and V along the $\text{Mg}_{1-x}\text{Fe}_x(\text{SO}_4) \cdot \text{H}_2\text{O}$ solid-solution series with linear regression lines. Errors are equal or smaller than the symbol size. The data for end-member kieserite are taken from Bechtold and Wildner (2016). Previous data for the Fe end-member (Wildner and Giester 1991) are shown (without errors) as dotted diamond symbols.

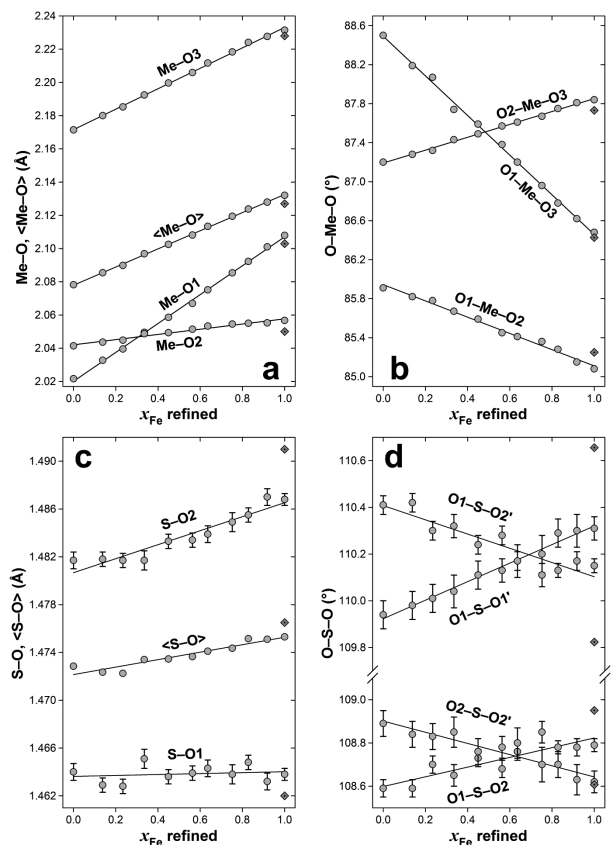


FIGURE 3. Polyhedral geometries along the $\text{Mg}_{1-x}\text{Fe}_x(\text{SO}_4) \cdot \text{H}_2\text{O}$ solid-solution series with linear regression lines. (a) Octahedral Me–O bond lengths and (b) O–Me–O angles, (c) tetrahedral S–O bond lengths, and (d) O–S–O angles. If not indicated, errors are equal or smaller than the symbol size. The data for end-member kieserite are taken from Bechtold and Wildner (2016). Previous data for the Fe end-member (Wildner and Giester 1991) are shown (without errors) as dotted diamond symbols.

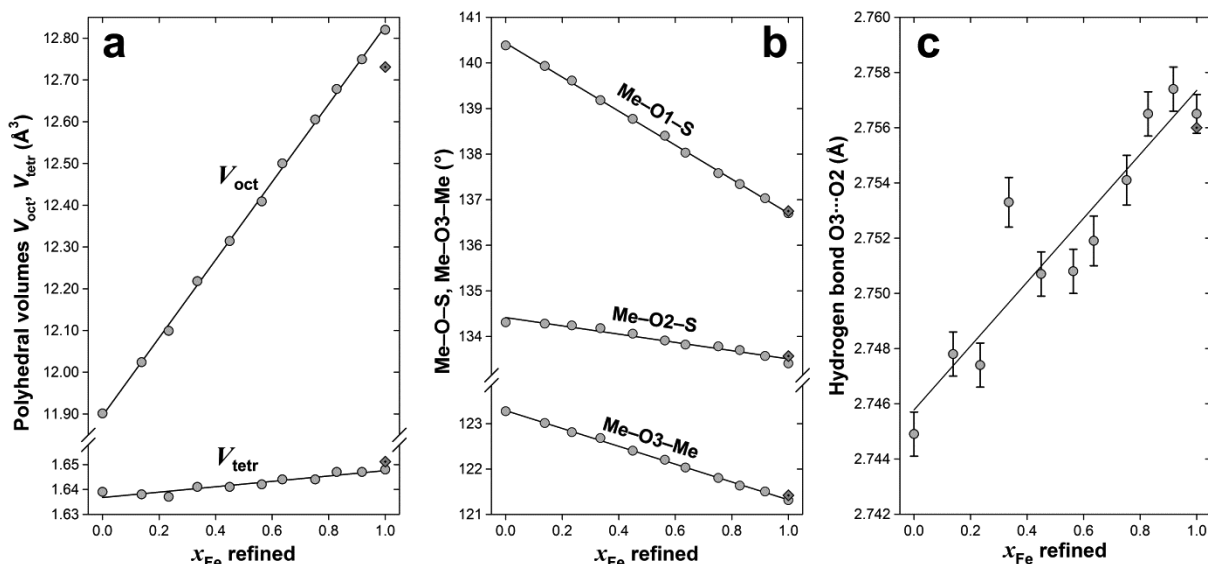


FIGURE 4. (a) Polyhedral volumes, (b) Me-O-S and Me-O-Me angles, and (c) hydrogen bond lengths along the $\text{Mg}_{1-x}\text{Fe}_x(\text{SO}_4) \cdot \text{H}_2\text{O}$ solid-solution series with linear regression lines. For **a**, note the strongly different scales for the tetrahedral and octahedral volumes. If not indicated, errors are equal or smaller than the symbol size. The data for end-member kieselite are taken from Bechtold and Wildner (2016). Previous data for the Fe end-member (Wildner and Giester 1991) are shown (without errors) as dotted diamond symbols.

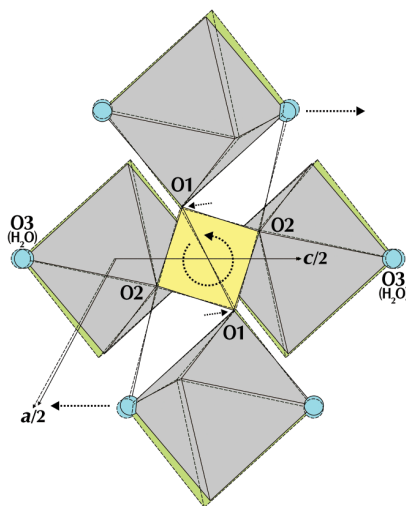


FIGURE 5. Overlay of crystal structure fragments of kieselite, $\text{MgSO}_4 \cdot \text{H}_2\text{O}$ (full lines), in front of szomolnokite, $\text{FeSO}_4 \cdot \text{H}_2\text{O}$ (dashed lines), centered at the S atom ($0, y, \frac{1}{4}$), in a projection along the negative b -axis. MgO₆ octahedra are shown in gray, FeO₆ octahedra below in green, SO₄ tetrahedra in yellow, and the water molecules as cyan spheres. Dotted arrows indicate major rotational and translational changes along the $\text{Mg}_{1-x}\text{Fe}_x(\text{SO}_4) \cdot \text{H}_2\text{O}$ solid-solution series as discussed in the text. Cell axes plots are scaled to 50%. Structural data for end-member kieselite are taken from Bechtold and Wildner (2016). (Color online.)

IR spectra

The IR spectra of the Mg/Fe monohydrated sulfates feature several clearly discernible absorption phenomena (Fig. 9). Taking as an example the FTIR spectra measured in transmission mode, the H₂O absorption region is dominated by a prominent

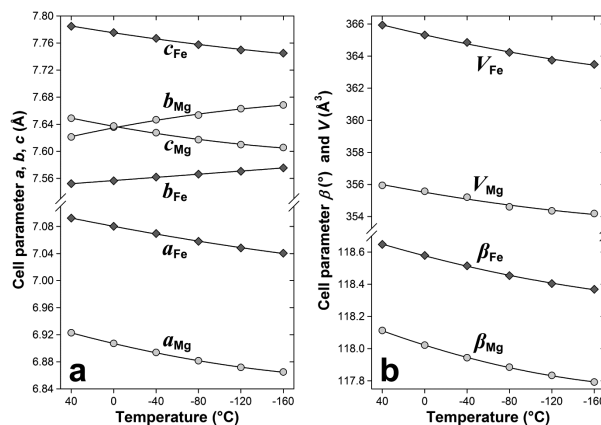


FIGURE 6. Variation of the lattice parameters (a) a , b , c and (b) β and V for kieselite ("Mg", light gray circle symbols) and szomolnokite ("Fe", dark gray diamond symbols) within the investigated temperature range, with second-order regression lines. Errors are equal or smaller than the symbol size.

band at $3182\text{--}3245\text{ cm}^{-1}$ ($3.14\text{--}3.08\text{ }\mu\text{m}$), representing the symmetric stretching vibration $\nu_{1(\text{H}_2\text{O})}$ of the H₂O molecule. A poorly resolved broad shoulder at even higher wavenumbers ($3367\text{--}3391\text{ cm}^{-1}/2.97\text{--}2.95\text{ }\mu\text{m}$) represents $\nu_{3(\text{H}_2\text{O})}$, the antisymmetric H₂O stretching mode. The H₂O bending vibration $\nu_{2(\text{H}_2\text{O})}$ occurs at $1525\text{--}1496\text{ cm}^{-1}$ ($6.56\text{--}6.68\text{ }\mu\text{m}$). A major band group (centered around $1150\text{ cm}^{-1}/8.70\text{ }\mu\text{m}$) corresponds to the anti-symmetric $\nu_{3(\text{SO}_4)}$ stretching mode of the sulfate tetrahedra and the IR-forbidden symmetric stretching mode $\nu_{1(\text{SO}_4)}$, visible as a weak but well-defined band around 1025 cm^{-1} . A pronounced absorption phenomenon (hereafter labeled "Peak 850 cm^{-1} "), considered as a potential diagnostic feature for monohydrated

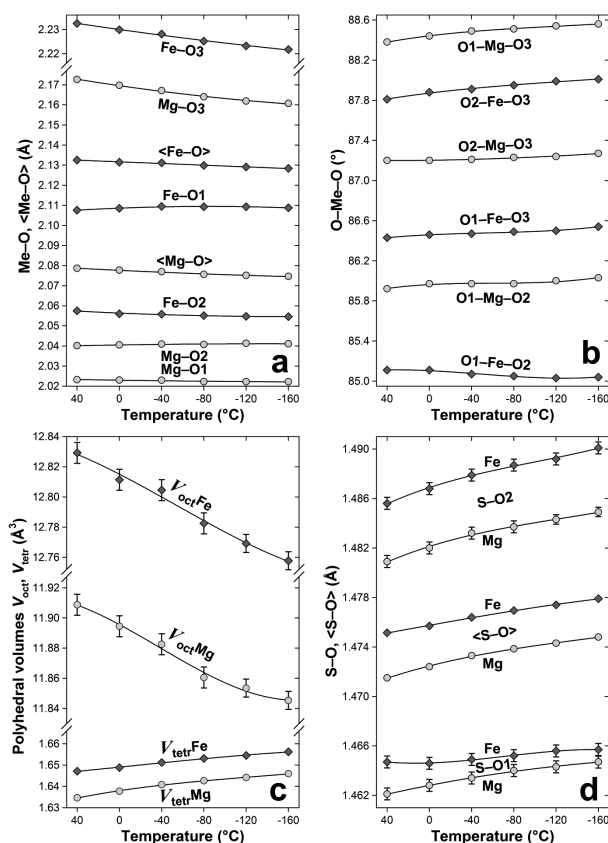


FIGURE 7. Variation of the polyhedral geometries (a) octahedral Me-O bond lengths and (b) O-Me-O angles, (c) polyhedral volumes, and (d) tetrahedral S-O bond lengths (uncorrected for thermal motion, see text) for kieserite (“Mg”, light gray circle symbols) and szomolnokite (“Fe”, dark gray diamond symbols) within the investigated temperature range, with second- or third-order regression lines. Third-order regressions are very probably not significant, but are used to guide the eye. For c, note the somewhat different scales for the tetrahedral and octahedral volumes. If not indicated, errors are equal or smaller than the symbol size.

kieserite-group sulfates by Lane (2007), occurs in our data (Fig. 9) at 884–831 cm^{-1} (11.31–12.03 μm). Last, a band group at 630 cm^{-1} (15.87 μm) is assigned to the $\nu_4(\text{SO}_4)$ bending modes.

It should be mentioned that the absorption band shape and even position vary significantly between individual FTIR measuring modes (Fig. 9). Nevertheless, the overall spectral appearance is comparable, with the absorption of the H_2O bending vibration $\nu_2(\text{H}_2\text{O})$ being enhanced in DRIFT spectra when using diluted sample material (Fig. 9). The sole exceptions as to the consistency of the spectral shapes are DRIFT measurements on pure sample material (no KBr dilution), where most intrinsic absorption phenomena at lower wavenumbers are suppressed, with strong artifacts present, such as the “reststrahlenband” labeled “R” in Figure 9, a pronounced absorption at around 1300 cm^{-1} . Absorptions due to H_2O modes at high wavenumbers are noisy, leading to the loss of resolution between the $\nu_1(\text{H}_2\text{O})$ and $\nu_3(\text{H}_2\text{O})$ bands. The spectral position of the reststrahlenband artifact, however, is also dependent on the sample composition, shifting from 1360 to 1283 cm^{-1} (7.35 to 7.78 μm) from kieserite to szomolnokite.

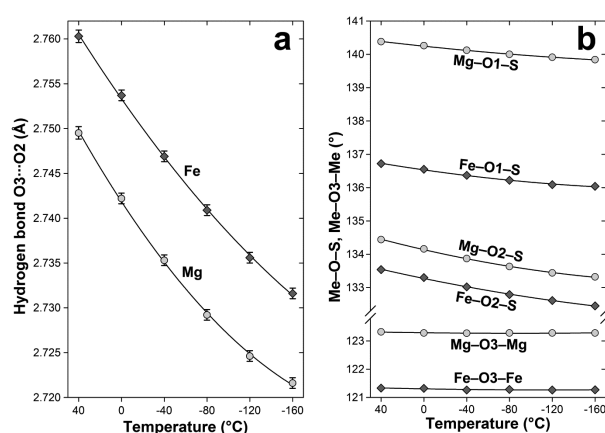


FIGURE 8. Variation of (a) hydrogen bond lengths and (b) Me-O-S/Me angles for kieserite (“Mg”, light gray circle symbols) and szomolnokite (“Fe”, dark gray diamond symbols) within the investigated temperature range, with second-order regression lines. If not indicated, errors are equal or smaller than the symbol size.

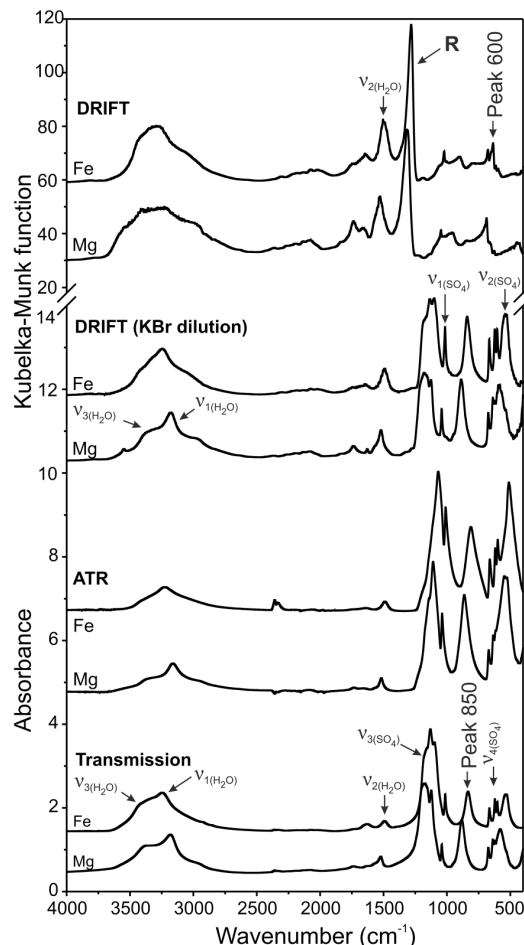


FIGURE 9. FTIR spectra of the kieserite and szomolnokite end-members, $\text{Mg/Fe}(\text{SO}_4) \cdot \text{H}_2\text{O}$, in each measuring mode. In addition to band position changes between the end-members, note the differences in band positions and shapes between the measuring modes.

A specific benefit of DRIFT measurements, however, is the enhanced amplitude of absorption bands assigned to H₂O combination modes in the 4400–5200 cm⁻¹ (2.27–1.92 μm) spectral region. Three distinct bands occur at 4688, 4845, and 5087 cm⁻¹ (2.13, 2.06, and 1.97 μm, respectively) in end-member kieserite. When x_{Fe} increases, both peripheral bands converge closer to the central one at 4845 cm⁻¹ (2.06 μm), creating the misleading impression (mainly in case of poor resolution or enhanced spectral noise) of a dominant single broad band at 4750 cm⁻¹ (2.10 μm) with a weaker one at 5025 cm⁻¹ (1.99 μm) in szomolnokite (Figs. 10a and 10b, Table 6).

In agreement with the structural behavior along the (Mg,Fe) SO₄·H₂O solid-solution series reported above, the positional changes of the IR absorption bands with increasing Fe content also show linear trends within limits of error (Fig. 11). The only exceptions to this rule are the above-mentioned H₂O combination modes seen in DRIFT spectra, where a more complex trend is observed. In many cases, the changes are quite subtle, such as for the position of the SO₄ vibrations and that of the H₂O bending mode, where the decrease in wavenumber from the kieserite to the szomolnokite end-member amounts to a mere 30 cm⁻¹ in all three measuring modes. Clearer correlation trends can be observed for the H₂O stretching vibrations, where the well-resolved ν₁(H₂O) band changes in position from 3182 in kieserite to 3245 cm⁻¹ in szomolnokite. A somewhat smaller but

still significant change can be seen for the apparent monohydrate sulfate diagnostic “Peak 850 cm⁻¹” (Lane 2007; Lane et al. 2015) that shifts in our data from 884 in kieserite to 831 cm⁻¹ with increasing x_{Fe} . No significant correlation could be observed for the ν₃(H₂O) band position, due to it being present as a mere shoulder of the afore-mentioned ν₁(H₂O) vibration, leading to significant fitting errors. The variations in the wavenumber position of relevant spectral absorption phenomena for the individual measurement modes, as well as the respective linear regression coefficients, are summarized in Table 6.

From the acquired temperature-dependent FTIR-spectra between +40 and -160/180 °C (Fig. 12), two opposite behaviors are evident. The sulfate tetrahedra behave as a rigid unit, which is reflected by the nearly stable position of all SO₄²⁻ vibrational modes regardless of temperature. On the contrary, the H₂O-related symmetric stretching vibration in kieserite shows a significant decrease in wavenumber by 29 cm⁻¹ (0.030 μm) from +40 °C down to -160 °C at a rate of -0.145 cm⁻¹/°C, and szomolnokite, measured down to -180 °C, shows a change of 33 cm⁻¹ (0.022 μm) with a comparable rate of -0.150 cm⁻¹/°C. The rate of decrease appears to be constant, independent of the Mg/Fe ratio (Fig. 12). The diagnostic “Peak 850 cm⁻¹” discussed earlier shows a wavenumber increase upon cooling, whereas

TABLE 6. Wavenumber positions of relevant absorption features in FTIR spectra in each measuring mode for the kieserite and szomolnokite end-members, Mg/Fe(SO₄)·H₂O at room temperature

Vibration	Wavenumber position (cm ⁻¹)		Linear regression coefficients ^a	
	Kieserite	Szomolnokite	a	b
Transmission (1:300 sample dilution in KBr)				
Peak 850 cm ⁻¹	884(1)	831(2)	-57.5(1)	887.8(8)
ν ₁ (SO ₄)	1043(1)	1015(1)	-29.6(1)	1040(1)
ν ₃ (SO ₄) _{main}	1165(1)	1133(1)	-27.8(1)	1162.1(8)
ν ₂ (H ₂ O)	1525(4)	1496(2)	-32.1(1)	1528.9(8)
ν ₁ (H ₂ O)	3182(4)	3245(4)	67.2(3)	3188(2)
ν ₃ (H ₂ O)	3367(12)	3391(10)	1.3(1)	3388(5)
Attenuated total reflectance (ATR)				
Peak 850 cm ⁻¹	866(3)	810(1)	-54.7(2)	861(1)
ν ₂ (H ₂ O)	1520(1)	1491(2)	-30.57(7)	1522.2(4)
ν ₁ (H ₂ O)	3165(4)	3217(5)	57.5(3)	3157(2)
ν ₃ (H ₂ O)	3345(8)	3340(10)	0.8(7)	3342(4)
Diffuse reflectance (1:20 sample dilution in KBr)				
Peak 850 cm ⁻¹	886(3)	839(1)	-57.2(2)	895.4(1)
ν ₁ (SO ₄)	1044(2)	1018(1)	-27.6(1)	1042(1)
ν ₃ (SO ₄) _{center}	1172(3)	1139(2)	-21.3(2)	1158(2)
ν ₂ (H ₂ O)	1523(1)	1494(1)	-29.38(6)	1523(4)
ν ₁ (H ₂ O)	3180(2)	3249(5)	70.8(2)	3180(1)
ν ₃ (H ₂ O)	3365(13)	3383(21)	1.7(6)	3359(3)
Diffuse reflectance (undiluted samples)				
Peak 600 cm ⁻¹	690(1)	678(1)	-11.6(1)	688.5(7)
Reststrahlenband	1316(6)	1283(5)	-30.1(2)	1312(1)
ν ₂ (H ₂ O)	1526(3)	1496(2)	-30.7(3)	1528(2)
ν ₁ (H ₂ O)	3203(20)	3304(9)	88.8(1)	3209(5)
ν ₃ (H ₂ O)	3412(23)	3431(9)	2.3(1)	3405(6)
Peak 4700 cm ⁻¹	4688(4)	4749(5)	—	—
Peak 4850 cm ⁻¹	4845(3)	4854(6)	—	—
Peak 5090 cm ⁻¹	5087(10)	5021(11)	—	—

Notes: Linear regression coefficients of the correlations between wavenumber and Fe content (x_{Fe}) are listed. Positions of weak yet important bands observed in the region of H₂O combination modes are given in the scope of DRIFT measurements on undiluted sample material.

^a Linear regression equation $y = a(x_{\text{Fe}}) + b$, where y denotes the wavenumber position of the vibration mode.

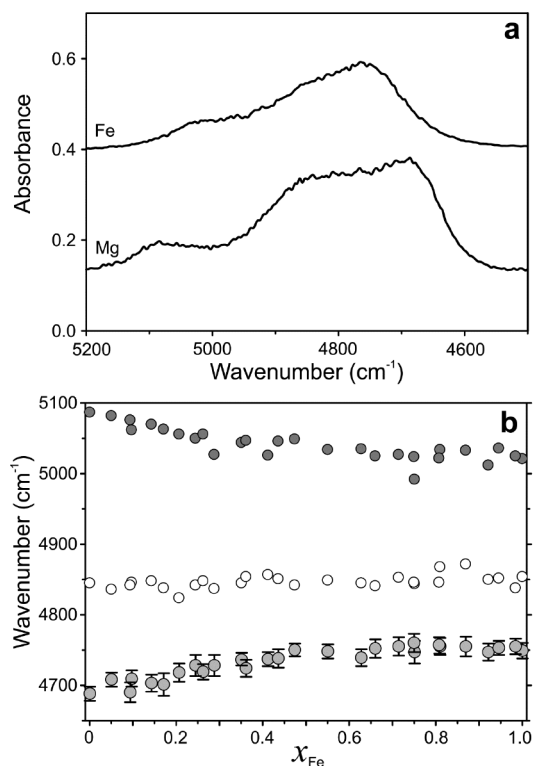


FIGURE 10. Spectral region with three diagnostic H₂O combination modes. (a) Observed in DRIFT measurements on undiluted sample material. (b) Detailed plot of band position change for the examined bands across the kieserite-szomolnokite solid-solution series. Errors equal or smaller than the symbol size are not plotted.

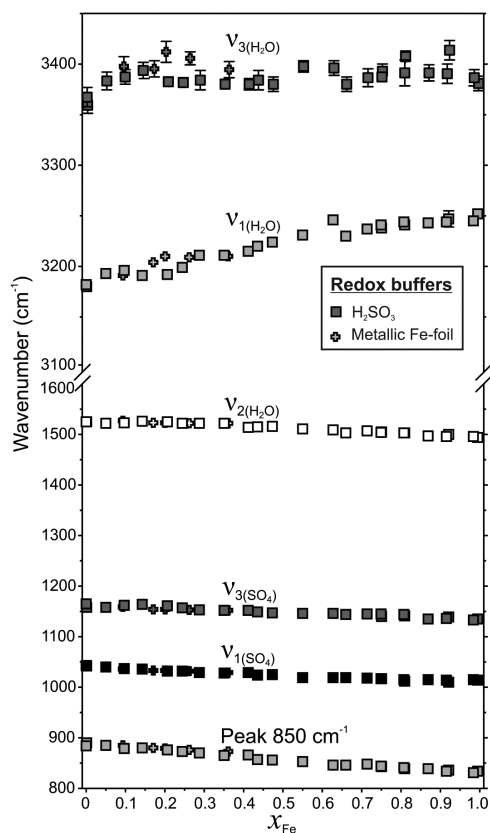


FIGURE 11. Dependence of the positions of relevant FTIR absorption features (transmission measurements) of $\text{Mg}_{1-x}\text{Fe}_x(\text{SO}_4) \cdot \text{H}_2\text{O}$ solid solutions on the Fe content at room temperature (RT). The scatter in data points of the $\nu_3(\text{H}_2\text{O})$ vibration is caused by the significant overlap with the $\nu_1(\text{H}_2\text{O})$ vibration. Errors equal or smaller than the symbol size are not plotted.

the H_2O bending vibration remains nearly unaffected by the temperature change.

Raman spectra

The changes in Raman band position along the kieserite–szomolnokite solid solution are also linear as could be expected from the FTIR results (Table 7). Figure 13 graphically depicts the positional changes of prominent bands across the solid-solution series in detail, and Table 7 gives the respective coefficients of the linear regression between the band position and x_{Fe} .

The Raman spectra consist of numerous narrow bands in the 100–1600 cm^{-1} shift region, with much better resolution compared to FTIR spectra (Fig. 9 vs. 14a). The most prominent band is the symmetric stretching vibration $\nu_1(\text{SO}_4)$ of the sulfate tetrahedron with Raman shift at 1042 cm^{-1} for kieserite and 1018 cm^{-1} for szomolnokite. Several relevant spectral features occur at lower shift values, and the most prominent ones are located at ~270, ~430, and a doublet at ~620 cm^{-1} . Weak bands in the spectral range 1100–1600 cm^{-1} are assigned to the split $\nu_3(\text{SO}_4)$ vibrations (Stoilova and Lutz 1998; Chio et al. 2007), with the exception of the broader H_2O bending mode at 1500 cm^{-1} . Stretching vibrations of the H_2O molecule occur in the expected region, i.e., the $\nu_1(\text{H}_2\text{O})$ band is located at 3179 up to 3247 cm^{-1} with

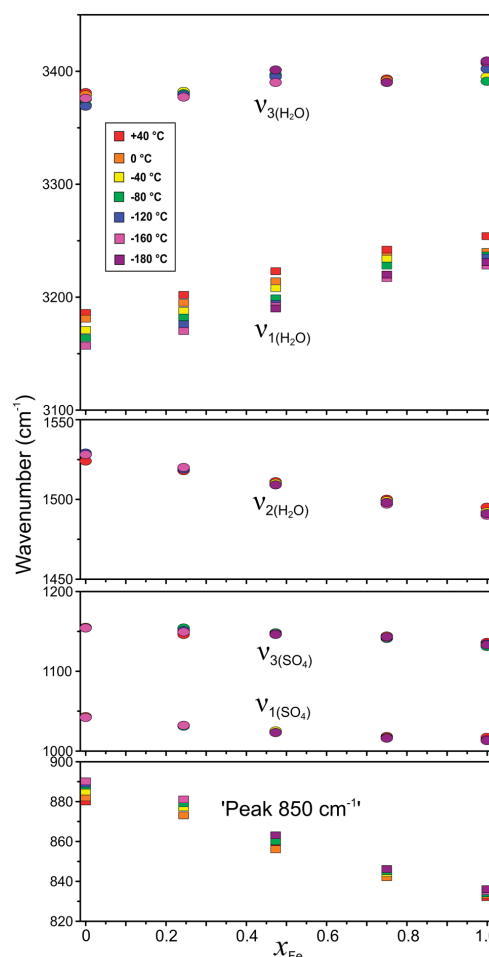


FIGURE 12. Dependence of the FTIR absorption band positions of $\text{Mg}_{1-x}\text{Fe}_x(\text{SO}_4) \cdot \text{H}_2\text{O}$ solid solutions on temperature, as seen in transmission mode. The two most promising candidate bands for the determination of x_{Fe} based on FTIR spectra are shown by rectangular symbols. (Color online.)

increasing x_{Fe} (Fig. 14b), whereas the antisymmetric $\nu_3(\text{H}_2\text{O})$ mode is again present as its shoulder, analogous to the FTIR spectra.

It should be mentioned that despite the sample being in finely powdered form, the effect of varying (and unknown) crystallite orientation, influencing the relative amplitude of the Raman bands, is clearly visible. This is attributed to the small scattering volume excited by the laser spot in comparison with the much higher (and thus orientation-averaging) sample volume measured by IR spectroscopic techniques (in the order of mm^3 , depending on the specific measuring mode). Fortunately, only band amplitudes are affected, while their positions remain the same.

Low-temperature Raman measurements have also been conducted. As expected, a significant composition-independent systematic shift of the band position with temperature is seen for the $\nu_1(\text{H}_2\text{O})$ band, which decreases in wavenumber shift by about 30 cm^{-1} across the full temperature range, and represents the strongest change among all examined bands. The $\nu_3(\text{H}_2\text{O})$ band is again poorly resolved, thus impeding any precise fit. The very good band resolution and low FWHM of the SO_4 vibrational

TABLE 7. Wavenumber shift positions of relevant bands in Raman spectra for the kieserite and szomolnokite end-members, $\text{Mg}/\text{Fe}(\text{SO}_4) \cdot \text{H}_2\text{O}$

Peak assignment	Raman shift position at RT (cm^{-1})		Linear regression coefficients ^a		Band shift with temperature decrease ($\times 10^{-2} \text{ cm}^{-1}/^\circ\text{C}$)
	Kieserite	Szomolnokite	a	b	
Lattice modes	125.3(1)	112.4(4)	-10.7(6)	123.7(3)	4.66
$\text{V}_{\text{transl}} \text{Fe}-\text{H}_2\text{O}$	219.2(1)	218.0(1)	-0.4(5)	219.2(3)	3.43
$\text{V}_2(\text{SO}_4)_1$	432.2(1)	422.8(1)	-9.4(3)	432.2(2)	-1.95
$\text{V}_2(\text{SO}_4)_2$	502.1(1)	493.8(1)	-7.2(3)	501.2(2)	-1.61
$\text{V}_4(\text{SO}_4)_1$	628.7(4)	616.6(2)	-11.78(4)	628.1(2)	0.85
$\text{V}_4(\text{SO}_4)_2$	633.8(2)	623(1)	-10.1(5)	633.0(3)	-0.55
$\text{V}_1(\text{SO}_4)$	1041.8(1)	1017.6(1)	-24.9(1)	1040.9(6)	-0.47
$\text{V}_3(\text{SO}_4)_1$	1101.6(1)	1071.0(5)	-28.7(1)	1101.2(8)	-1.82
$\text{V}_3(\text{SO}_4)_2$	1118.9(1)	1090.4(7)	-29.1(1)	1121(1)	-0.51
$\text{V}_3(\text{SO}_4)_3$	1216.7(1)	1195.0(1)	-22.0(9)	1215(5)	2.22
$\text{V}_2(\text{H}_2\text{O})$	1508.3(1)	1477.6(1)	-27.1(3)	1501(2)	2.22
$\text{V}_1(\text{H}_2\text{O})$	3178(2)	3247(5)	53.0(6)	3189(4)	-16.57
$\text{V}_3(\text{H}_2\text{O})$	3388(4)	3368(12)	-9(1)	3372(6)	15.25

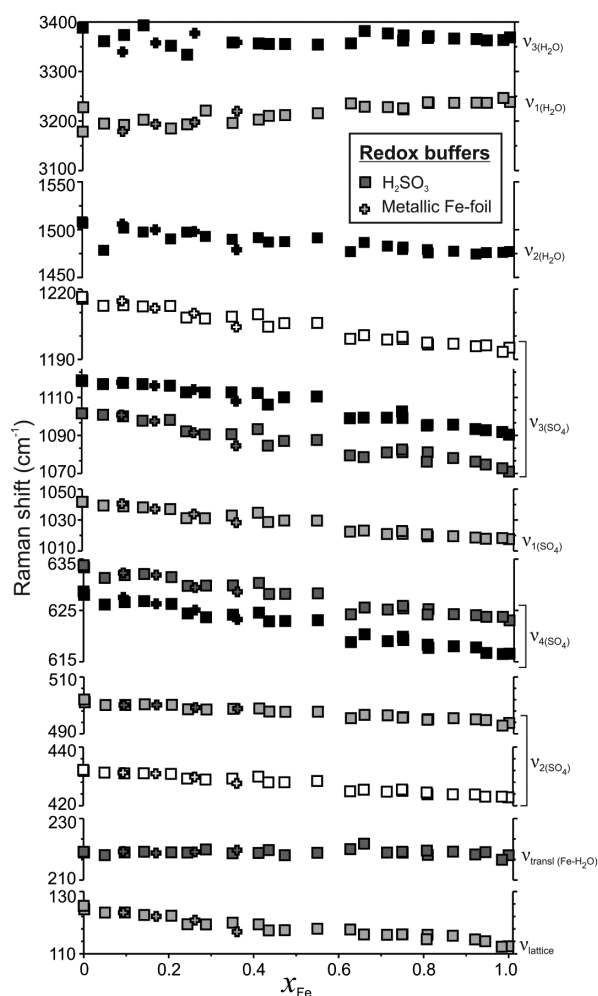
Notes: Linear regression coefficients of the correlations between band position and the Fe content (x_{Fe}) are listed. Additionally, changes in the band position with decreasing temperature are given for all relevant Raman bands.

^a Linear regression equation $y = a(x_{\text{Fe}}) + b$, where y denotes the Raman shift position.

bands in Raman spectra allow accurate examination of even their subtle positional changes, which are not so apparent in IR spectra (Table 7). In general, their wavenumber change with temperature never exceeds 10 cm^{-1} within the examined temperature range (Table 7). A systematic increase in wavenumber shift is observed at low temperature for the lowest-energetic bands, representing octahedral stretching modes according to Chio et al. (2007). For all observed bands, the rates at which the band positions change with temperature remain constant across the examined temperature range, allowing one to determine a mean shift per 1°C for the individual bands, listed in Table 7.

UV-Vis-NIR spectroscopy and crystal field calculations

The optical absorption spectrum of szomolnokite is shown in Figure 15. Two prominent crystal field absorption bands centered around 7650 and 10640 cm^{-1} are attributed to transitions from the $^5\text{T}_{2g}$ ground state with parental ^5D term to the spin-allowed $^5\text{E}_g(\text{D})$ level of octahedral Fe^{2+} , which is split into two non-degenerate states in non-cubic crystal fields (i.e., in a pseudo-tetragonal approach $^5\text{A}_g$ and $^5\text{B}_g$). A sharp peak at 6565 cm^{-1} within the low-energy wing of the first crystal field band represents the first overtone of the O–H stretching mode. All other spectral features observed between 19800 to 25900 cm^{-1} (see inset in Fig. 15) are very weak and can be attributed to spin-forbidden crystal field transitions of Fe^{2+} derived from excited triplet terms, very probably $^3\text{T}_g(\text{H})$, $^3\text{T}_g(\text{G})$, $^3\text{E}_g(\text{H})$, $^3\text{T}_g(\text{G})$, and $^3\text{T}_g(\text{F}_2)$, in sequence of increasing energy (labels for cubic symmetry). The background increase in absorption toward the UV is most likely related to the LMCT transition (ligand–metal charge transfer) of trace contents of Fe^{3+} , causing the light beige hue of szomolnokite. The crystal field (CF) calculations, either based on a full superposition model (SM) calculation in the actual triclinic polyhedral symmetry, or on a pseudotetragonal approach assuming a $[4+2]$ -elongated octahedron and employing classical CF parameters, both yield basically comparable and reasonable results, summarized in Table 8. They also match well with respective results for cobaltkieserite (Wildner 1996), showing

**FIGURE 13.** Dependence of the Raman band positions of $\text{Mg}_{1-x}\text{Fe}_x(\text{SO}_4) \cdot \text{H}_2\text{O}$ solid solutions on the Fe content x_{Fe} at room temperature. Errors are equal or smaller than the symbol size.

the comparability of crystal fields in transition metal kieserite-group compounds. Apart from similar field strengths Dq_{cub} and Racah parameters, even the tetragonal distortion parameter Dt , expressing the polyhedral elongation of the $\text{H}_2\text{O}-\text{Me}-\text{OH}_2$ axis, is similarly underestimated due to the higher field strength of H_2O molecules compared to oxygen ligands of the SO_4 groups.

DISCUSSION

Crystal structural evolution and crystal chemistry

In view of previous single-crystal structure investigations of end-member kieserite (Bechtold and Wildner 2016; earlier Hawthorne et al. 1987) and szomolnokite (Wildner and Giester 1991), the solid-solution series presented here behaves as expected: in particular, all lattice parameters and crystal chemical data exhibit Vegard-type behavior within the limits of error, i.e., they show linear changes with Mg/Fe ratio. The extent of those changes along the solid solution allows, among others, to infer the Mg/Fe ratio in $\text{Mg}_{1-x}\text{Fe}_x\text{SO}_4 \cdot \text{H}_2\text{O}$ samples of unknown composition from X-ray data. Furthermore, this work also constitutes an important

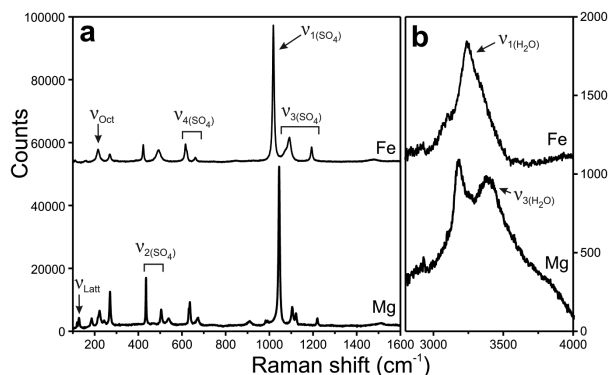


FIGURE 14. Raman spectra of the kieserite and szomolnokite end-members, $\text{Mg/Fe}(\text{SO}_4) \cdot \text{H}_2\text{O}$, at room temperature.

basis for any further theoretical calculations of interest, as well as the possibility to easily determine the values of thermodynamic parameters for any member of the solid solution. This is enabled because the Vegard-type behavior indicates one-site ideal mixing of both end-members (Powell and Holland 1993). Enthalpy, entropy, molar volume, as well as heat capacity and thermal expansion can be determined by the linear combination of these parameters for both end-members in their respective formula ratio in the sample (van Hinsberg et al. 2005a, 2005b).

As expected from a crystal chemical point of view, the replacement of the smaller Mg cation ($r_{\text{Mg}} = 0.720 \text{ \AA}$) by the larger Fe^{2+} ($r_{\text{Fe}^{2+}} = 0.780 \text{ \AA}$; all radii from Shannon 1976) leads to a corresponding increase of average and individual Me–O bond lengths, of the respective octahedral volume, and hence also of the unit-cell volume (Figs. 2b, 3a, and 4a). However, a more detailed analysis is advisable, since this is not the case for the

TABLE 8. Summary of results from classical crystal field (CF) and superposition model (SM) calculations for Fe^{2+} in szomolnokite, based on observed transition energies as indicated in Figure 15

Szolnokite	SM (triclinic)	"Classical" CF (tetragonal)
Dq_{cub}	–	855
Dq_{eq}	–	878
Dt	–	40
Ds	–	660
Racah B ($C/B = 4.3$)	835	840
β ($B_0 = 897 \text{ cm}^{-1}$)	0.93	0.94
Dq_{cub} (from s_4)	826	855
B_4	4920	–
B_2	8900	–
s_4	7573	7838
s_2	2319	2066

Notes: Fixed SM parameters are $R_0 = 2.13 \text{ \AA}$, $t_4 = 5$, $t_2 = 3$. All given values are in cm^{-1} except the ratio C/B (fixed at 4.3) and the nephelauxetic ratio β . Racah B_0 and C/B are taken from Figgis and Hitchman (2000).

kieserite–cobaltkieserite solid-solution series, $\text{Mg}_{1-x}\text{Co}_x\text{SO}_4 \cdot \text{H}_2\text{O}$, recently studied by Bechtold and Wildner (2016). There, the replacement of the smaller Mg by the larger Co^{2+} ($r_{\text{Co}^{2+}} = 0.745 \text{ \AA}$) leads to an increase of average and individual Me–O bond lengths and of the octahedral volume, but surprisingly at the same time the cell volume is reduced. Apart from Bechtold and Wildner (2016) (and earlier Wildner and Giester 1991 and Giester and Wildner 1992) for kieserite-type compounds, a comparable aberrant behavior has been explicitly noted and documented for blödite-type compounds $\text{Na}_2\text{Me}^{2+}(\text{SO}_4)_2 \cdot 4\text{H}_2\text{O}$ (Stoilova and Wildner 2004) or for Tutton's salts $\text{K}_2\text{Me}^{2+}(\text{SO}_4)_2 \cdot 6\text{H}_2\text{O}$ (Bosi et al. 2009). Bechtold and Wildner (2016) attribute this mismatch to the absence of (for Mg) and the presence of (for Co^{2+}) $3d$ orbitals, the latter imposing anisotropy of the electron density around transition metal (TM) cations. This anisotropy affects the position of the bond critical point r_c along the Me–O

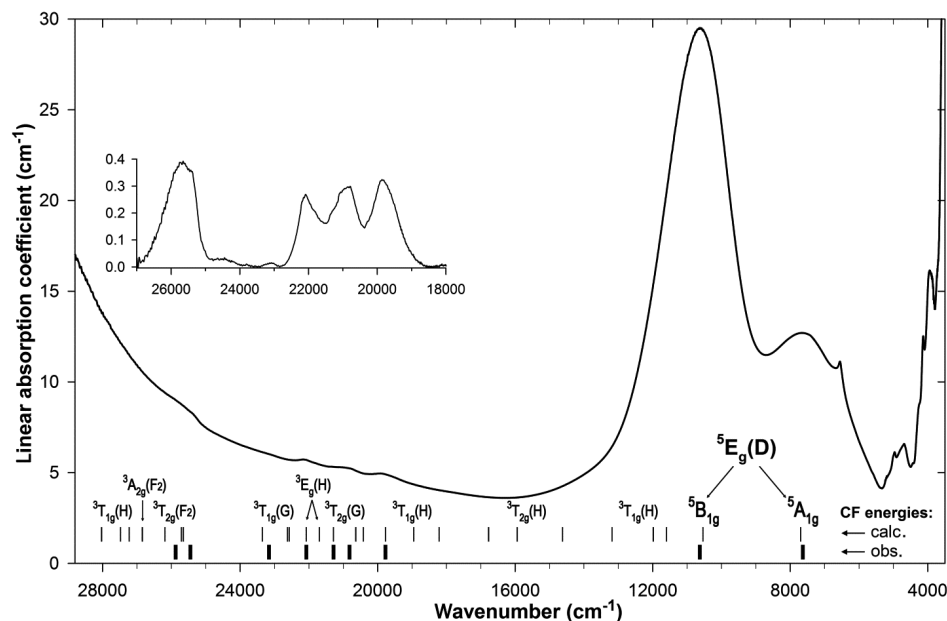


FIGURE 15. UV-Vis-NIR absorption spectrum of szomolnokite in the range from 28 800–3500 cm^{-1} with observed (bold line marks) and calculated energy levels (thin line marks) and respective assignments for cubic symmetry, in case of spin-allowed ${}^5E_g(D)$ also with tetragonal labels. Calculated singlet states are not shown. The inset shows the background-subtracted and intensity-enhanced region between 27 000–18 000 cm^{-1} .

bond path and the electron density $\rho(\mathbf{r}_c)$ at this point (cf. e.g., Bader 1998). For Mg–O bonds, \mathbf{r}_c lies comparatively closer to Mg with lower $\rho(\mathbf{r}_c)$ than for 3dTM–O bonds, thus in turn also affecting the electron density at the oxygen ligands and hence the second coordination sphere: S–O bond lengths (slightly) increase with Co- and in the present case Fe-uptake (Fig. 3c); however, the second coordination sphere “contracts” due to increased interpolyhedral folding as evidenced by reduction of the Me–O–S and Me–O–Me angles shown in Figure 4b (also see respective discussion, figures, and references in Bechtold and Wildner 2016). These aspects are also directly related to significant differences in the total, as well as Me^{2+} -cation polarizabilities α in kieserite compared to the 3dTM kieserite-group compounds, as recently discussed by Gagné et al. (2018) for various structure types comprising Mg- and 3dTM-representatives. All the arguments discussed for Co^{2+} also hold for Fe^{2+} compared to Mg, but due to the clearly higher difference in ionic radii, no eye-catching volume mismatch is found for the present kieserite–szomolnokite solid-solution series.

Nonetheless, szomolnokite (and Fe-rich representatives in general) also deviates in some aspects from the otherwise uniform properties of kieserite and the 3dTM-kieserite-group sulfates, especially concerning the tendency toward a [2+2+2]-coordination in the octahedral unit, compared to clear [4+2] geometries in the kieserite-group monohydrate sulfates of Mg, Mn, Ni, Co, and Zn (see Fig. 2 in Wildner and Giester 1991). Hence we may suppose that a moderately elongated octahedral [4+2]-environment complies well with packing requirements of the kieserite structure type (note that a strong elongation imposed, e.g., by Jahn-Teller affected Cu^{2+} is not accepted, leading to symmetry reduction; Giester 1988). The deviation observed for szomolnokite might be attributed to the uneven *d*-electron distribution of high-spin 3d⁶-configured Fe^{2+} , with one excess (i.e., paired) electron in the triply degenerate t_{2g} set of the 3d orbitals. Other representatives have either no (for Mg), symmetrically (for Mn^{2+} , Ni^{2+}) or fully occupied (for Zn^{2+}) 3d orbitals, or two excess (paired) electrons in the t_{2g} orbital set (as for Co^{2+}). In the latter case, an appropriately elongated [4+2] Jahn-Teller distortion is theoretically expected, neglecting any thermodynamic considerations (in practice, respective static effects are not statistically detectable in room-temperature crystal structures; Wildner 1992). However, in case of 3d⁶-configured Fe^{2+} , a compressed octahedral [2+4] Jahn-Teller distortion is theoretically predicted, thus suggesting the specific uneven *d*-electron distribution as probable explanation for the particular deviation of the octahedral distortion in szomolnokite (but there seem to exist no systematic studies seeking to generally verify a respective static effect for Fe^{2+}).

IR, Raman, and crystal field spectra

IR spectra at ambient conditions. The linear Vegard-type behavior observed in the structural data of the $\text{Mg}_{1-x}\text{Fe}_x\text{SO}_4 \cdot \text{H}_2\text{O}$ solid-solution series (Figs. 2–4) is also reflected in the results of FTIR and Raman spectroscopic measurements. With wavenumber units in use, one can recognize a linear change of the position of IR spectral bands across the kieserite–szomolnokite series (Fig. 11, Table 6). Evidently, the wavenumber of the prominent symmetric stretching vibration $\nu_{1(\text{H}_2\text{O})}$ of the H_2O molecule increases with Fe content. This is in agreement with

the structural data (Fig. 4c, Table 4), where the O3···O2 donor–acceptor hydrogen bond length increases with x_{Fe} , expectably leading to the observed band behavior (e.g., Libowitzky 1999). Likewise, a similar blue-shift of the antisymmetric stretching mode $\nu_{3(\text{H}_2\text{O})}$ would also be expected. However, since the band overlaps significantly with the prominent $\nu_{1(\text{H}_2\text{O})}$ absorption, the trend is obscured due to reduced fitting accuracy. The H_2O bending mode $\nu_{2(\text{H}_2\text{O})}$ decreases slightly but constantly in position with increasing x_{Fe} , which might be correlated with the widening of the acceptor–donor–acceptor angle O2···O3···O2 from kieserite to szomolnokite (136.7–140.5°). Both the symmetric $\nu_{1(\text{SO}_4)}$ vibration and the three bands assigned to the split $\nu_{3(\text{SO}_4)}$ mode (Chio et al. 2007; Lane 2007) decrease in wavenumber with increasing x_{Fe} , in accord with the observed slight relaxation of the SO_4^{2-} tetrahedron toward szomolnokite (Figs. 3c and 4a, Table 4). Of the latter three bands, only the major one is depicted, and its position followed in Figure 11 and Table 6 since the peripheral bands present as shoulders are not traceable reliably. Similar to $\nu_{1(\text{H}_2\text{O})}$, the prominent “Peak 850 cm^{-1} ” absorption band deemed as diagnostic by Lane (2007) and Lane et al. (2015) could also be used to infer the Mg/Fe ratio, since it shows a pronounced wavenumber decrease toward Fe-rich compositions (i.e., 831 cm^{-1} in szomolnokite). A group of bands at ~630 cm^{-1} , assigned by Lane et al. (2015) to the $\nu_{4(\text{SO}_4)}$ vibration, cannot easily be exploited for cosmochemical considerations, as the spectral region not only consists of numerous bands with varying FWHM but also does not prove to be clearly discernible from the signals of other sulfates and even silicates. Furthermore, the martian atmosphere is dominated by CO_2 that has a strong band centered at ~667 cm^{-1} , potentially obscuring bands within the wings of the CO_2 band (~529 to 794 cm^{-1} ; e.g., Christensen et al. 2000). Therefore, the IR spectral region between 700 and 300 cm^{-1} (14.3–27.0 μm) was not studied in further detail.

In contrast, the 4400–5200 cm^{-1} (2.27–1.92 μm) spectral region, where absorptions associated with combination modes of the H_2O stretching and bending modes occur, is considered by many authors to be an important spectral feature in reflectance spectra from Mars orbiters, allowing not only to discern kieserite from other sulfate hydrates, in which the prominent bands occur at higher wavenumbers (Mangold et al. 2008; Noel et al. 2015), but also to roughly infer its Fe content (Cloutis et al. 2007; Bishop et al. 2009; Liu et al. 2016). The H_2O combination modes are most apparent in DRIFT spectra of pure undiluted sample material. The kieserite end-member shows a typical set of three bands at ~4700, 4850, and 5090 cm^{-1} (2.13, 2.06, and 1.96 μm) (Figs. 10a and 10b, Table 6). A comparison between the kieserite and szomolnokite end-member patterns (Bishop et al. 2009) has led many of the above-mentioned authors to infer the presence of a single dominant absorption band (2.09 μm) with a shoulder in szomolnokite, instead of the clearly visible triplet observed in kieserite. As can be seen in Figure 10a, all three bands occur in szomolnokite as well, with the peripheral bands “converged” in their position closer to the central one. Given their broad FWHM, the three bands, shifted close together in szomolnokite, create the misleading impression of a broad peak (central band) with a single shoulder (highest-energetic peak) with the center at a higher wavenumber than the strongest of the three individual bands discernible in end-member kieserite, which corresponds

to the lowest-energetic peak in the triplet (Fig. 10a, Table 6). A more detailed analysis of the behavior of the triplet with increasing x_{Fe} revealed a nonlinear relation of the band position with the Mg/Fe ratio at higher Fe contents. This discrepancy may, however, be attributed to the presence of a weak yet broad band caused by Fe^{2+} crystal field transitions (Fig. 15), which partly alters the background even in the H_2O combination mode region due to its large FWHM (Jamieson et al. 2014). Together with the H_2O -related combination bands being very weak even when measuring undiluted sample material in DRIFT mode, a fitting error is introduced, which, to our opinion, accounts for the non-linearity of the observed trends when higher amounts of Fe^{2+} are present (Fig. 10b, Table 6).

As noted above, the wavenumber of any particular absorption in the IR spectrum also changes in relation to the measuring technique (Table 6). As an example, the $\nu_{1(\text{H}_2\text{O})}$ band occurs at 3182 cm^{-1} in end-member kieserite measured in transmission mode, whereas the corresponding feature is centered at 3165 cm^{-1} in ATR mode and as high as 3203 cm^{-1} using the DRIFT technique on the very same sample (3.14, 3.16, and $3.12\text{ }\mu\text{m}$, respectively). The shift in band position may be attributed to the known change in refractive index close to a spectral absorption, dependent on the ratio of the reflection and transmission components constituting the final spectral signal. Besides, DRIFT spectra of undiluted sample material show significant artifacts (reststrahlenband, etc.) instead of the expected sulfate vibrations between 1300 and 370 cm^{-1} (7.69 and $27.02\text{ }\mu\text{m}$). A sample dilution of 1:20 in an IR-transparent material (KBr) already leads to a spectral shape very close to the result of proper transmission measurements, with enhanced amplitudes of weaker bands, such as $\nu_{2(\text{H}_2\text{O})}$ and the H_2O combination modes.

All these factors have implications for measurements on Mars, where IR spectra reflected by “fluffy” kieserite aggregates (more transmission) would somewhat differ in shape and band position from signals acquired on compact kieserite masses or crusts due to the different reflection/transmission ratio of the particular material. Disregard of these issues could be misleading in the assessment of the properties and composition of the measured monohydrate sulfate. On the other hand, the grain size seems to have little effect on the band position in IR reflectance spectra (Jamieson et al. 2014; Pitman et al. 2014).

With this in mind, promising spectral features for a semi-quantitative assessment of the chemistry of kieserite-group solid solutions from orbiter spectra should be the absorption bands with a pronounced regression slope in relation to x_{Fe} . In addition to the H_2O combination mode region centered at $\sim 4900\text{ cm}^{-1}$ ($2.04\text{ }\mu\text{m}$), a promising candidate would seem to be the $\nu_{1(\text{H}_2\text{O})}$ band, showing a wavenumber change toward higher values by $\sim 60\text{ cm}^{-1}$ ($0.06\text{ }\mu\text{m}$) from kieserite to szomolnokite (Fig. 11). While $\nu_{2(\text{H}_2\text{O})}$ and the sulfate modes all show smaller positional changes with respect to sample chemistry, the “Peak 850 cm^{-1} ” ($11.8\text{ }\mu\text{m}$), deemed as diagnostic for monohydrated sulfates by previous authors (Lane et al. 2015), appears to be promising as well due to a comparatively large shift in wavenumber of roughly 50 cm^{-1} ($0.72\text{ }\mu\text{m}$).

When expressing positions and shifts of the spectral bands (e.g., as done just above), a “technical” issue immediately becomes apparent. The choice of spectral units, i.e., wavenumber in cm^{-1} vs. wavelength in micrometers, significantly influences

the shape of the spectral envelope and the apparent extent of changes in the position of absorption features. Whereas the difference in the wavenumber position of the H_2O symmetric stretching mode $\nu_{1(\text{H}_2\text{O})}$ and the “Peak 850 cm^{-1} ” band amounts to a comparable shift of 60 and 50 cm^{-1} , respectively, the same values expressed in wavelength as spectral unit amount to 0.06 and $0.72\text{ }\mu\text{m}$, respectively, setting both values apart by an entire order of magnitude. While wavelength units are more commonly used in the Vis-NIR research of the cosmochemical community, wavenumber units were chosen for this work because it better suits our aim of comparing the structural and spectroscopic behavior of the kieserite–szomolnokite solid-solution series. Unlike wavelength, wavenumber units are directly proportional to the frequency and thus to the energy of the observed phonons, allowing for a meaningful comparison with structural data. Furthermore, IR spectra represented in wavenumber units facilitate band fitting using Voigt profiles, as the absorption bands appear symmetrical, unlike the situation with wavelength units (especially $>4\text{ }\mu\text{m}$). In this way, we were able to amply demonstrate the linear Vegard-type dependency of vibrational bands on the interatomic distances and polyhedral size along the entire kieserite–szomolnokite solid solution and the consistency of single-crystal X-ray and spectral results. Furthermore, the direct comparison of related vibrational features between Raman and IR spectra is simplified. The corresponding wavelengths λ (in μm) can be easily obtained according to the formula $\lambda(\mu\text{m}) = 10000/\nu(\text{cm}^{-1})$.

Temperature dependence of IR spectra. Temperature-related spectral changes (Fig. 12) are important to consider, especially for interpreting extraterrestrial data, e.g., from Mars, where the average temperature spans from $+20$ to $-120\text{ }^\circ\text{C}$ (Witzke et al. 2007) and reaches values as low as 5 K elsewhere. Considering that the two bands showing the strongest change with increasing Fe content ($\nu_{1(\text{H}_2\text{O})}$ and “Peak 850 cm^{-1} ”) are also those showing the greatest variation in position with temperature (Fig. 12), the range of error in the assessment of x_{Fe} from a single band can be up to ± 0.25 without the approximate knowledge of temperature. The same, considering the temperature sensitivity of the fundamental H_2O bands, will apply to their combination modes in the $\sim 4900\text{ cm}^{-1}$ region (Figs. 10a and 10b), which, according to the results for kieserite of Jamieson et al. (2014), split further apart with decreasing temperature. This behavior is in contrast to the “merging” of the three bands from kieserite to szomolnokite into a seemingly single broad absorption at higher wavenumbers. In contrast to $\nu_{1(\text{H}_2\text{O})}$, the H_2O bending vibration hardly changes with temperature, obviously related to the small change of the acceptor–donor–acceptor angle $\text{O}2\cdots\text{O}3\cdots\text{O}2$ ($\sim 1.6^\circ$), compared to the significant influence of the Mg/Fe ratio ($\sim 4^\circ$).

As to the sulfate bands, the splitting of $\nu_{3(\text{SO}_4)}$ into three components and the low amplitude of the $\nu_{1(\text{SO}_4)}$ symmetric stretching vibration are the effects that hamper precise fitting and estimation of x_{Fe} , not temperature, toward which they are insensitive.

Raman spectra at ambient conditions. Raman spectra acquired across the solid solution also exhibit systematic band shifts with variable x_{Fe} (Figs. 13 and 14, Table 7), and corresponding vibrational modes show the same behavior in IR and Raman spectra. However, the better band resolution due to narrower FWHMs and fewer band overlaps in Raman spectra allow for

a more precise refinement of the subtle changes in position and splitting of the diverse SO_4 modes, as well as a more accurate characterization of octahedral modes with changing Mg/Fe ratio.

The increase in hydrogen bond length with increasing x_{Fe} leads to the expected increase in the wavenumber of the H_2O symmetric stretching vibration from 3179 to 3247 cm^{-1} shift (3.14–3.08 μm). The nearly perfect match between the positions observed in the IR transmission spectra and the Raman data underline the consistency of both data sets.

The change in position of the $\nu_{1(\text{SO}_4)}$ vibration from 1042 to 1018 cm^{-1} between kieserite and szomolnokite, respectively, also parallels its behavior in the IR spectra, where it was present, albeit weak (e.g., Fig. 11; Lane 2007). On the contrary, it represents the strongest feature in the Raman spectra of the kieserite–szomolnokite solid solutions, making it the optimum candidate to infer the Mg/Fe ratio, more so given its stable position at lower temperatures (see below). Also, the three well-resolved bands assigned to the split antisymmetric $\nu_{3(\text{SO}_4)}$ vibration offer a more accurate insight into the behavior of the sulfate tetrahedron, in that the spectral positions of all three modes tend to decrease with increasing x_{Fe} , as noted before by other methods. The same holds true for the wavenumber decrease of the other modes of the SO_4 group (Fig. 13, Table 7), in accord with its slight relaxation upon Fe uptake revealed by the single-crystal diffraction data (Figs. 3c and 3d, Table 4). The bands observed in the 100–250 cm^{-1} shift region feature a component at $\sim 220 \text{ cm}^{-1}$ assigned by Chio et al. (2007) to a vibration involving the translation along the Fe– H_2O bond. However, its spectral position remains nearly unchanged regardless of the Mg/Fe ratio (Fig. 13, Table 7), which challenges this assignment, given the variation in octahedral bond lengths across the solid solution (Table 4). A significant positional decrease was observed for the lowest mode at $\sim 130 \text{ cm}^{-1}$, changing from 137 to 112 cm^{-1} from kieserite to szomolnokite. While we are unable to ascertain the exact character of this vibration, its significant change with the Mg/Fe ratio makes it another viable band to infer on the chemistry of kieserite-group minerals from vibrational spectra.

Temperature dependence of Raman spectra. Band shifts in low-temperature Raman spectra show similar behavior to that of the corresponding vibrational modes observed in the IR spectra (Table 7). Better band resolution compared to IR spectra allows, however, to accurately track even the subtle positional changes of sulfate-related peaks. The highest-energy peak of the split $\nu_{3(\text{SO}_4)}$ mode at $\sim 1200 \text{ cm}^{-1}$ increases, while the lowest-energy $\nu_{3(\text{SO}_4)}$ peak at $\sim 1100 \text{ cm}^{-1}$ decreases in position (Table 7). This increase of spectroscopic distortion may be correlated with the slight increase in geometric tetrahedral distortion at reduced temperatures (compare respective distortion parameters in Tables 4 and 5).

The vibrational mode at $\sim 220 \text{ cm}^{-1}$ shift shows a notable increase in wavenumber at low temperature. This behavior, together with its position at $\sim 220 \text{ cm}^{-1}$, implies a possibility that the diagnostic “Peak 850 cm^{-1} ” absorption feature in the IR spectra (Lane et al. 2015), is actually a combination of this mode and the $\nu_{4(\text{SO}_4)}$ mode at $\sim 630 \text{ cm}^{-1}$, which decreases in wavenumber from kieserite to szomolnokite. This would lead to the expected wavenumber decrease of the resulting IR absorption at $\sim 850 \text{ cm}^{-1}$ from kieserite to szomolnokite, as would be dictated by the trends seen for both $\nu_{4(\text{SO}_4)}$ components (Fig. 13). The absence of this band in the Raman spectra supports this theory since

such phenomena are suppressed in Raman spectroscopy to a great extent due to the different underlying physical process of spectrum formation (IR absorption vs. inelastic scattering). The splitting of the $\nu_{4(\text{SO}_4)}$ vibration into two bands may also account for the slight asymmetry observed for the “Peak 850 cm^{-1} ” IR band (Fig. 13, Table 7).

Use of vibrational spectra to infer the composition of martian kieserite. Linear trends, observed for changes in structural parameters of $(\text{Mg,Fe})\text{SO}_4 \cdot \text{H}_2\text{O}$ (Figs. 2–4), as well as in the position of IR bands (when expressed in wavenumbers) and in Raman spectra, clearly correlate with the Mg/Fe ratio (Figs. 11 and 13). Aside from documenting in detail the behavior of kieserite-group compounds throughout the Mg/Fe solid-solution series, the linearity of the data also allows its use as a standard in evaluating IR spectra acquired during orbiter missions as well as Raman measurements, which will be conducted during future rover missions to Mars.

In general, the evaluation of OMEGA (0.35 to 5.2 μm) and CRISM (0.362 to 3.92 μm) measurements in the VNIR-SWIR spectral range (visible/near to shortwave infrared) leading to the assessment of the mineral phases present on the planet’s surface and their composition, follows the “spectral unmixing” approach, requiring reference end-member spectra (Cloutis et al. 2006; Combe et al. 2008; Mangold et al. 2008; Bishop et al. 2009; Lichtenberg et al. 2010; Roach et al. 2010; Noel et al. 2015; Liu et al. 2016). In brief, using the reference end-member spectra, the spectral signal from orbiter measurements is fitted by least-squares techniques, after its correction for the instrumental function (CRISM smile, etc.), atmospheric scattering and incidence angle, using a detailed knowledge of Mars topography simultaneously verified by MOLA (Mars Orbital Laser Altimeter). While to date, only pure end-member kieserite and szomolnokite spectra were used for this assessment, the detection of linear trends across the entire kieserite–szomolnokite solid solution presented in this work allows us to derive reference spectra for kieserite–szomolnokite solid solution minerals of intermediate composition and, in theory, to then obtain additional information on the chemistry (i.e., Mg/Fe ratio) of the unknown $(\text{Mg,Fe})\text{SO}_4 \cdot \text{H}_2\text{O}$ kieserite-group mineral at hand, with semi-quantitative results.

However, additional sources of error arise from the use of different correction data sets preceding the actual spectral unmixing procedure. Different versions of the atmospheric correction model used in the evaluation of CRISM spectra may lead to significant changes in the form of the resulting spectrum, even causing errors in the discrimination between kieserite and szomolnokite end-members in the same region of interest. Such a case can be seen comparing the work of Bishop et al. (2009) to that of Noel et al. (2015), when the latter dismissed the presence of Fe-rich kieserite or end-member szomolnokite in Juventae Chasma using a newer parameter set. We nevertheless believe that at least a semi-quantitative impression as to the Mg/Fe ratio in kieserite-group minerals in a studied region can be obtained from IR spectra, as long as comparable correction routines are used.

As already outlined above, the knowledge of surface temperatures (at least approximate values) during remote measurements facilitates quantitative comparisons, but otherwise useful semi-

quantitative information (better than $x_{\text{Fe}} \pm 0.25$) may be extracted, especially when combining several spectral features. The attempt to use sulfate-related bands for such considerations is hampered by their wavenumber position being largely insensitive to temperature changes in IR spectra (Fig. 12). Given the limited resolution of orbiter spectra up to date, this will likely prevent any exact observation of the subtle band position changes due to enhanced noise.

A much more promising situation is to be expected considering the higher resolution and low FWHM of Raman bands, which aids in ascertaining their position changes from kieserite to szomolnokite with higher precision. The superior spectral resolution even allows efficient use of the sulfate-related bands, such as the prominent $\nu_{1(\text{SO}_4)}$ band (Fig. 14), to infer the Mg/Fe content, with the benefit of their nearly perfect insensitivity to temperature changes. Despite the lack of surface Raman data at the moment, forthcoming rover missions (in particular ExoMars 2020 and Mars 2020) include Raman on-board instruments. Besides, Mars rovers are and will be equipped with thermometers, providing the precise temperature during the measurement.

This work considers the behavior of kieserite and szomolnokite, as we know it from Earth, i.e., crystallizing in the above described $C2/c$ structure type. However, a second “polymorph” of $\text{MgSO}_4 \cdot \text{H}_2\text{O}$ has been postulated in literature to be present as a stable phase instead of or along with “classic” kieserite on Mars. This phase has been obtained during dehydration-rehydration studies at Mars-relevant conditions by Wang et al. (2009, 2011) and is often labeled LH-kieserite (LH for “low humidity”); Jamieson et al. (2014) obtained this “polymorph” by dehydrating kieserite at 250 °C for one week. The resulting phase shows minor spectral differences compared to “classic” kieserite, with a slightly different position of the H_2O combination modes in the 4900 cm^{-1} (2.04 μm) region. We are currently working on a paper elucidating the actual character and spectroscopic properties of this second kieserite “polymorph” in detail.

Crystal field spectra. The main purpose of presenting an optical crystal field (CF) spectrum of szomolnokite in the present context is to provide an impression on the possible influence of the spin-allowed ${}^5\text{T}_{2g}(\text{D}) \rightarrow {}^5\text{E}_g(\text{D})$ crystal field transition of octahedral Fe^{2+} on remote or in situ NIR spectra from orbiter and rover missions. Figure 15 shows that the cubic ${}^5\text{E}_g(\text{D})$ state splits into two levels in the low-symmetry field of szomolnokite and that the lower energy ${}^5\text{A}_{1g}$ split level (tetragonal label) centered at 7650 cm^{-1} (1.31 μm) may influence overtones and combinations modes in the NIR spectra from ~5350 cm^{-1} (1.87 μm) onward. In particular, the first overtone of the H_2O stretching mode is located at 6565 cm^{-1} within the low-energy wing of ${}^5\text{A}_{1g}$, also perceivable in the VNIR DRIFT spectra of szomolnokite acquired by Pitman et al. (2014). Concerning CF states, up to now only the higher-energetic and more intense ${}^5\text{B}_{1g}$ split level at 10640 cm^{-1} (0.94 μm) was attributed to szomolnokite (at 0.9–0.95 μm) and discussed (Cloutis et al. 2006; Bishop et al. 2009; Jamieson et al. 2014; Pitman et al. 2014). It was argued that the latter Fe-related absorption (~0.95 μm) is commonly observed in spectra of martian sulfate salts and thus may not uniquely identify szomolnokite, since it could also be produced by even minor amounts of particles of a separate Fe-bearing dust phase covering sulfate rocks (Bishop et al. 2009). However, the ${}^5\text{A}_{1g}$ split level at 7640 cm^{-1} (1.31 μm) was not considered so

far as diagnostic for szomolnokite, in spite of the fact that it is present, albeit weak, also in the comparative laboratory spectra of szomolnokite by Bishop et al. (2009). Furthermore, in the usual wavelength presentation, this band is broadened compared to the stronger ${}^5\text{B}_{1g}$ band and thus even less noticeable. Admittedly, in Fe-bearing monohydrated sulfate, i.e., in diluted szomolnokite, the electronic ${}^5\text{A}_{1g}$ band will be most likely too weak to be extracted from orbiter spectra, but we propose to regard it as highly diagnostic for szomolnokite in data of future rover missions. Moreover, since the energies of the ${}^5\text{E}_g(\text{D})$ split levels at 7650 and 10640 cm^{-1} are very closely reproduced by the CF calculations at 7713 and 10549 cm^{-1} , respectively (full triclinic SM calculation, Table 8), the influence of temperature as well as of the Mg/Fe ratio in solid solutions can be efficiently predicted from our presented single-crystal structure data: for example, a temperature reduction to –160 °C hardly changes the calculated energy of ${}^5\text{B}_{1g}$ (10539 cm^{-1}) but predicts a moderate shift of ${}^5\text{A}_{1g}$ by ~100 cm^{-1} to 7815 cm^{-1} ; In contrast, stronger band shifts are predicted with changing Mg/Fe ratio: for the structure with $\text{Mg}_{0.55}\text{Fe}_{0.45}$ (Tables 1 and 4; Supplemental Table S1) respective energies of 11034 and 8249 cm^{-1} are calculated for ambient conditions.

IMPLICATIONS

The verification of the existence of a continuous solid-solution series between kieserite and szomolnokite suggests that respective intermediate compositions are expected to occur in Fe-rich environments. The presented data can generally assist in the identification of kieserite, szomolnokite, and their solid solutions and not only on Mars, despite the attention given to this planet. The linear character of the observed spectral and structural trends at room temperature and the knowledge of their changes upon cooling provide a solid starting basis to draw conclusions about the composition of this important martian sulfate based on absorption band positions in IR and Raman spectra. Even in the case of a semi-quantitative approach (no knowledge of temperature), zoning of Fe contents in martian kieserite-containing sediments can be monitored. The presented data are especially relevant in view of the shortly forthcoming rover missions Mars 2020 (NASA) and ExoMars 2020 (ESA) allowing in situ vibrational spectroscopic measurements, including, for the first time on Mars, Raman investigations.

Chemical zoning of kieserite-group minerals from past spectral results may also be determined. Promising candidates for such a re-evaluation are, as representative examples, the spatially resolved CRISM spectra acquired across the large Ius Chasma and Juventae Chasma sulfate deposits or Aram Chaos.

ACKNOWLEDGMENTS AND FUNDING

We sincerely thank Melissa D. Lane and an anonymous reviewer for their detailed and thorough comments and opinions, which helped to significantly improve the quality and readability of this paper. Assistance by G. Giester (Vienna) with the low-temperature X-ray data collections is gratefully acknowledged. We also thank R. Miletich, M. Ende, and J. Meusbürger (all Vienna) for helpful discussions, and P. Kadlec of the Masaryk University (Brno) for the chemical analyses of our samples. M.W. is grateful to Y.Y. Yeung (Hong Kong) for providing a modified copy of his HCFLDN2 program. This work was supported by a grant from the Austrian Science Fund (FWF): P 29149-N29.

REFERENCES CITED

- Arvidson, R.E., Poulet, F., Bibring, J.-P., Wolff, M., Gendrin, A., Morris, R.V., Freeman, J.J., Langevin, Y., Mangold, N., and Belucci, G. (2005) Spectral

- reflectance and morphologic correlations in eastern Terra Meridiani, Mars. *Science*, 307, 1591–1594.
- Bader, R.F.W. (1998) Atoms in Molecules. In P.v.R. Schleyer, Ed., *Encyclopedia of Computational Chemistry* vol 1, 64–86. Wiley, Chichester.
- Bechtold, A., and Wildner, M. (2016) Crystal chemistry of the kieserite–cobalt-kieserite solid solution, $\text{Mg}_{1-x}\text{Co}_x(\text{SO}_4) \cdot \text{H}_2\text{O}$: well behaved oddities. *European Journal of Mineralogy*, 28, 43–52.
- Beegle, L.W., Bhartia, R., DeFlores, L., Darrach, M., Kidd, R.D., Abbey, W., Asher, S., Burton, A., Clegg, S., Conrad, P.G., and others. (2014) SHERLOC: Scanning Habitable Environments with Raman & Luminescence for Organics & Chemicals, an investigation for 2020. 11th International GeoRaman Conference, 5101 (pdf).
- Bishop, J.L., Parente, M., Weitz, C.M., Noe Dobrea, E.Z., Roach, L.H., Murchie, S.L., McGuire, P.C., McKeown, N.K., Rossi, C.M., Brown, A.J., and others. (2009) Mineralogy of Juventae Chasma: Sulfates in the light-toned mounds, mafic minerals in the bedrock, and hydrated silica and hydroxylated ferric sulfate on the plateau. *Journal of Geophysical Research*, 114, E00D09.
- Bosi, F., Belardi, G., and Ballirano, P. (2009) Structural features in Tutton's salts $\text{K}_2[\text{M}^{2+}(\text{H}_2\text{O})_6(\text{SO}_4)_2]$, with $\text{M}^{2+} = \text{Mg}, \text{Fe}, \text{Co}, \text{Ni}, \text{Cu}$, and Zn . *American Mineralogist*, 94, 74–82.
- Brese, N.E., and O'Keeffe, M. (1991) Bond-valence parameters for solids. *Acta Crystallographica*, B47, 192–197.
- Brown, I.D., and Shannon, R.D. (1973) Empirical bond–strength–bond–length curves for oxides. *Acta Crystallographica*, A29, 266–282.
- Chang, Y.M., Rudowicz, C., and Yeung, Y.Y. (1994) Crystal field analysis of the $3d^n$ ions at low symmetry sites including the “imaginary” terms. *Computers in Physics*, 8, 583–588.
- Chio, C.H., Sharma, S.K., and Muenow, D.W. (2007) The hydrates and deuterates of ferrous sulfate (FeSO_4): a Raman spectroscopic study. *Journal of Raman Spectroscopy*, 38, 87–99.
- Christensen, P.R., Bandfield, J.L., Clark, R.N., Edgett, K.S., Hamilton, V.E., Hoefen, T., Kieffer, H.H., Kuzmin, R.O., Lane, M.D., Malin, and others. (2000) Detection of crystalline hematite mineralization on Mars by the Thermal Emission Spectrometer: Evidence for near-surface water. *Journal of Geophysical Research*, 105, 9623–9642.
- Christensen, P.R., Wyatt, M.B., Glotch, T.D., Rogers, A.D., Anwar, S., Arvidson, R.E., Bandfield, J.L., Blaney, D.L., Budney, C., Calvin, W.M., and others. (2004) Mineralogy at Meridiani Planum from the Mini-TES experiment on the Opportunity rover. *Science*, 306, 1733–1739.
- Clark, B.C., and Van Hart, D.C. (1981) The salts of Mars. *Icarus*, 45, 370–378.
- Clark, B.C., Morris, R.V., McLennan, S.M., Gellert, R., Joliff, B., Knoll, A.H., Squyres, S.W., Lowenstein, T.K., Ming, D.W., Tosca, N.J., Yen, A., and others. (2005) Chemistry and mineralogy of outcrops at Meridiani Planum. *Earth and Planetary Science Letters*, 240, 73–94.
- Cloutis, E.A., Craig, M.A., Mustard, J.F., Kruzevsky, R.V., Jamroz, W.R., Scott, A., Bish, D.L., Poulet, F., Bibring, J.-P., and King, P.L. (2007) Stability of hydrated minerals on Mars. *Geophysical Research Letters*, 34, L20202.
- Combe, J.-Ph., Le Mouélic, S., Sotin, C., Gendrin, A., Mustard, J.F., Le Deit, L., Launeau, P., Bibring, J.-P., Gondet, B., Langevin, Y., and Pinet, P. (2008) Analysis of OMEGA/Mars Express hyperspectral data using a Multiple-Endmember Linear Spectral Unmixing Model (MELSUM): Methodology and first results. *Planetary and Space Science*, 56, 951–975.
- Dobrolenskiy, Y.S., Korablev, O.I., Fedorova, A.A., Mantsevich, S.N., Kalinnikov, Y.K., Vyazovetskiy, N.A., Titov, A.Y., Stepanov, A.V., Sapgir, A.G., Alexandrov, K.V., and others. (2017) Spectrometer ISEM for ExoMars-2020 space mission. *European Planetary Science Congress Abstracts*, 11, 255.
- Downs, R.T., Gibbs, G.V., Bartelme, K.L., and Boisen, M.B. Jr. (1992) Variations of bond lengths and volumes of silicate tetrahedra with temperature. *American Mineralogist*, 77, 751–757.
- Dyar, M.D., and Schaefer, M.W. (2004) Mössbauer spectroscopy on the surface of Mars: constraints and expectations. *Earth and Planetary Science Letters*, 218, 243–259.
- Dyar, M.D., Breves, E., Jawin, E., Marchand, G., Nelms, M., O'Connor, V., Peel, S., Rothstein, Y., Sklute, E.C., Lane, M.D., Bishop, J.L., and Mertzman, S.A. (2013) Mössbauer parameters of iron in sulfate minerals. *American Mineralogist*, 98, 1943–1965.
- Feldman, W.C., Mellon, M.T., Maurice, S., Prettyman, T.H., Carey, J.W., Vaniman, D.T., Bish, D.L., Fialipis, C.I., Chipera, S.J., Kargel, J.S., and others. (2004) Hydrated states of MgSO_4 at equatorial latitudes on Mars. *Geophysical Research Letters*, 31, L16702.
- Figgis, B.N., and Hitchman, M.A. (2000) *Ligand Field Theory and its Applications*, 364 p. Wiley-VCH.
- Gagné, O., Hawthorne, F.C., Shannon, R.D., and Fischer, R.X. (2018) Empirical electronic polarizabilities: deviations from the additivity rule. I. $\text{M}^{2+}\text{SO}_4 \cdot n\text{H}_2\text{O}$, blödite $\text{Na}_2\text{M}^{2+}(\text{SO}_4)_2 \cdot 4\text{H}_2\text{O}$, and kieserite-related minerals with sterically strained structures. *Physics and Chemistry of Minerals*, 45, 303–310.
- Gendrin, A., Mangold, N., Bibring, J.-P., Langevin, Y., Gondet, B., Poulet, F., Bonello, G., Quantin, C., Mustard, J., Arvidson, R., and Le Mouélic, S. (2005) Sulfates in Martian layered terrains: the OMEGA/Mars Express view. *Science*, 307, 1587–1591.
- Giester, G. (1988) The crystal structures of $\text{CuSO}_4 \cdot \text{H}_2\text{O}$ and $\text{CuSeO}_4 \cdot \text{H}_2\text{O}$, and their relationships to kieserite. *Mineralogy and Petrology*, 38, 277–284.
- Giester, G., and Wildner, M. (1992) The crystal structures of kieserite-type compounds. II. Crystal structures of $\text{Me}(\text{II})\text{SeO}_4 \cdot \text{H}_2\text{O}$ ($\text{Me} = \text{Mg}, \text{Mn}, \text{Co}, \text{Ni}, \text{Zn}$). *Neues Jahrbuch Mineralogischer Monatshefte*, 1992, 135–144.
- Glotch, T.D., Bandfield, J.L., Christensen, P.R., Calvin, W.M., McLennan, S., Clark, B.C., Rogers, A.D., and Squyres, S.W. (2006) Mineralogy of the light-toned outcrop at Meridiani Planum as seen by the Miniature Thermal Emission Spectrometer and implications for its formation. *Journal of Geophysical Research*, 111, E12S03.
- Griffen, D.T., and Ribbe, P.H. (1979) Distortions in the tetrahedral oxyanions of crystalline substances. *Neues Jahrbuch für Mineralogischer Abhandlungen*, 137, 54–73.
- Hawthorne, F.C., Groat, L.A., Raudsepp, M., and Ercit, T.S. (1987) Kieserite, $\text{Mg}(\text{SO}_4)(\text{H}_2\text{O})$, a titanite-group mineral. *Neues Jahrbuch für Mineralogischer Abhandlungen*, 157, 121–132.
- Jamieson, C.S., Noe Dobrea, E.Z., Dalton, J.B. III, Pitman, K.M., and Abbey, W.Z. (2014) The spectral variability of kieserite ($\text{MgSO}_4 \cdot \text{H}_2\text{O}$) with temperature and grain size and its application to the Martian surface. *Journal of Geophysical Research: Planets*, 119, 1218–1237.
- Karunatillake, S., Wray, J.J., Gasnault, O., McLennan, S.M., Rogers, A.D., Squyres, S.W., Boynton, W.V., Skok, J.R., Ojha, L., and Olsen, N. (2014) Sulfates hydrating bulk soil in the Martian low and middle latitudes. *Geophysical Research Letters*, 41, 7987–7996.
- Keil, K., Clark, B.C., Baird, A.K., Toulmin, P. III, and Rose, H.J.J. (1978) Zur Chemie der Marsoberfläche. *Mineralogische und petrologische Implikationen. Naturwissenschaften*, 65, 231–238.
- Knauth, L.P., Burt, D.M., and Wohletz, K.H. (2005) Impact origin of sediments at the Opportunity landing site on Mars. *Nature*, 438, 1123–1128.
- Lane, M.D. (2007) Mid-infrared emission spectroscopy of sulfate and sulfate-bearing minerals. *American Mineralogist*, 92, 1–18.
- Lane, M.D., Bishop, J.L., Dyar, M.D., Hiroi, T., Mertzman, S.A., Bish, D.L., King, P.L., and Rogers, A.D. (2015) Mid-infrared emission spectroscopy and visible/near-infrared reflectance spectroscopy of Fe-sulfate minerals. *American Mineralogist*, 100, 66–82.
- Libowitzky, E. (1999) Correlation of O–H stretching frequencies and O–H···O hydrogen bond lengths in minerals. *Monatshefte für Chemie*, 130, 1047–1059.
- Lichtenberg, K.A., Arvidson, R.E., Morris, R.V., Murchie, S.L., Bishop, J.L., Fernández-Remolar, D., Glotch, T.D., Dobrea, E.N., Mustard, J.F., Andrews-Hanna, J., and Roach, L.H. (2010) Stratigraphy of hydrated sulfates in the sedimentary deposits of Aram Chaos, Mars. *Journal of Geophysical Research*, 115, E00D17.
- Liu, Y., Glotch, T.D., Scudder, N.A., Kraner, M.L., Condu, T., Arvidson, R.E., Guinness, E.A., Wolff, M.J., and Smith, M.D. (2016) End-member identification and spectral mixture analysis of CRISM hyperspectral data: A case study on southwest Melas Chasma, Mars. *Journal of Geophysical Research: Planets*, 121, 2004–2036.
- Mangold, N., Gendrin, A., Gondet, B., Le Mouélic, S., Quantin, C., Ansan, V., Bibring, J.-P., Langevin, Y., Masson, P., and Nukum, G. (2008) Spectral and geologic study of the sulfate-rich region of West Candor Chasma, Mars. *Icarus*, 194, 519–543.
- Milliken, R.E., Mustard, J.F., Poulet, F., Jouglet, D., Bibring, J.-P., Gondet, B., and Langevin, Y. (2007) Hydration state of the Martian surface as seen by Mars Express OMEGA: 2. H_2O content of the surface. *Journal of Geophysical Research*, 112, E08S07.
- Morrison, S.M., Downs, R.T., Blake, D.F., Prabhu, A., Eleish, A., Vaniman, D.T., Ming, D.W., Rampe, E.B., Hazen, R.M., Achilles, C.N., and others. (2018) Relationships between unit-cell parameters and composition for rock-forming minerals on Earth, Mars, and other extraterrestrial bodies. *American Mineralogist*, 103, 848–856.
- Noel, A., Bishop, J.L., Al-Samir, M., Gross, C., Flahaut, J., McGuire, P.C., Weitz, C.M., Seelos, F., and Murchie, S. (2015) Mineralogy, morphology and stratigraphy of the light-toned interior layered deposits at Juventae Chasma. *Icarus*, 251, 315–331.
- Nonius (1998) Kappa CCD program package. Nonius B.V., Delft.
- Papike, J.J., Burger, P.V., Karner, J.M., and Shearer, C.K. (2007) Mars surface mineralogy: Implications of kieserite group crystal chemistry ($\text{Mg}, \text{Fe}^{2+}, \text{Mn}^{2+}, \text{Zn}, \text{Ni}, \text{Co})\text{SO}_4 \cdot \text{H}_2\text{O}$. 7th International Conference on Mars, 3004 (pdf).
- Pitman, K.M., Noe Dobrea, E.Z., Jamieson, C.S., Dalton, J.B. III, Abbey, W.J., and Joseph, E.C.S. (2014) Reflectance spectroscopy and optical functions for hydrated Fe-sulfates. *American Mineralogist*, 99, 1593–1603.
- Powell, R., and Holland, T. (1993) On the formulation of simple mixing models for complex phases. *American Mineralogist*, 78, 1174–1180.
- Roach, L.H., Mustard, J.F., Swayze, G., Milliken, R.E., Bishop, J.L., Murchie, S.L., and Lichtenberg, K. (2010) Hydrated mineral stratigraphy of Ius Chasma, Valles Marineris. *Icarus*, 206, 253–268.
- Robinson, K., Gibbs, G.V., and Ribbe, P.H. (1971) Quadratic elongation: a quantitative measure of distortion in coordination polyhedra. *Science*, 172, 567–570.
- Rull, F. (2018) Mars mineralogy: The EXOMARS 2020 approach. *Acta Crystal-*

- lographica, A74, e55.
- Rull, F., Maurice, S., Hutchinson, I., Morat, A., Perez, C., Diaz, C., Colombo, M., Belenguer, T., Lopez-Reyes, G., Sansano, A., and others. (2017) The Raman laser spectrometer for the ExoMars rover mission to Mars. *Astrobiology*, 17, 627–654.
- Schröder, C., Klingelhöfer, G., and Tremel, W. (2004) Weathering of Fe-bearing minerals under Martian conditions, investigated by Mössbauer spectroscopy. *Planetary and Space Science*, 52, 997–1010.
- Shannon, R.D. (1976) Revised effective ionic radii and systematic studies of interatomic distances in halides and chalcogenides. *Acta Crystallographica*, A32, 751–767.
- Sheldrick, G.M. (2008) A short history of SHELX. *Acta Crystallographica*, A64, 112–122.
- Stoilova, D., and Lutz, H.D. (1998) Infrared study of ν_{OD} modes in isotopically dilute (HDO) kieserite-type compounds $\text{MXO}_4 \cdot \text{H}_2\text{O}$ ($\text{M}=\text{Mn}, \text{Co}, \text{Ni}, \text{Zn}$, and $\text{X}=\text{S}, \text{Se}$) with matrix-isolated M^{2+} and $\text{X}'\text{O}_4^{2-}$ guest ions. *Journal of Molecular Structure*, 450, 101–106.
- Stoilova, D., and Wildner, M. (2004) Blödite-type compounds $\text{Na}_2\text{Me}^{2+}(\text{SO}_4)_2 \cdot 4\text{H}_2\text{O}$ ($\text{Me} = \text{Mg}, \text{Co}, \text{Ni}, \text{Zn}$): Crystal structures and hydrogen bonding systems. *Journal of Molecular Structure*, 706, 57–63.
- van Hinsberg, V.J., Vriend, S.P., and Schumacher, J.C. (2005a) A new method to calculate end-member thermodynamic properties of minerals from their constituent polyhedra I: enthalpy, entropy and molar volume. *Journal of Metamorphic Geology*, 23, 165–179.
- (2005b) A new method to calculate end-member thermodynamic properties of minerals from their constituent polyhedra II: heat capacity, compressibility and thermal expansion. *Journal of Metamorphic Geology*, 23, 681–693.
- Wang, A., Freeman, J.J., and Jolliff, B.L. (2009) Phase transition pathways of the hydrates of magnesium sulfate in the temperature range 50°C to 5°C: Implication for sulfates on Mars. *Journal of Geophysical Research*, 114, E04010.
- Wang, A., Freeman, J.J., Chou, I.-M., and Jolliff, B.L. (2011) Stability of Mg-sulfates at –10°C and the rates of dehydration/rehydration processes under conditions relevant to Mars. *Journal of Geophysical Research*, 116, E12006.
- Wiens, R.C., Maurice, S., and Rull Perez, F.P. (2017a) The SuperCam remote sensing instrument suite for the Mars 2020 rover: A preview. *Spectroscopy*, 32, 50–55.
- Wiens, R.C., Newell, R., Clegg, S., Sharma, S.K., Misra, A., Bernardi, P., Maurice, S., McCabe, K., Cais, P., and the SuperCam Science Team (2017b) The SuperCam remote Raman spectrometer for Mars 2020. *Lunar and Planetary Science XLVIII*, 2600 (pdf).
- Wildner, M. (1992) On the geometry of $\text{Co(II)}\text{O}_6$ polyhedra in inorganic compounds. *Zeitschrift für Kristallographie*, 202, 51–70.
- (1996) Polarized electronic absorption spectra of Co^{2+} ions in the kieserite-type compounds $\text{CoSO}_4 \cdot \text{H}_2\text{O}$ and $\text{CoSeO}_4 \cdot \text{H}_2\text{O}$. *Physics and Chemistry of Minerals*, 23, 489–496.
- Wildner, M., and Giester, G. (1991) The crystal structures of kieserite-type compounds. I. Crystal structures of $\text{Me(II)SO}_4 \cdot \text{H}_2\text{O}$ ($\text{Me} = \text{Mn}, \text{Fe}, \text{Co}, \text{Ni}, \text{Zn}$). *Neues Jahrbuch für Mineralogischer Monatshefte*, 296–306.
- Wildner, M., Beran, A., and Koller, F. (2013) Spectroscopic characterisation and crystal field calculations of varicoloured kyanites from Loliondo, Tanzania. *Mineralogy and Petrology*, 107, 289–310.
- Witzke, A., Arnold, G., and Stöffler, D. (2007) Spectral detectability of Ca- and Mg-sulphates in Martian bright soils in the 4–5 μm wavelength range. *Planetary and Space Science*, 55, 429–440.

MANUSCRIPT RECEIVED JANUARY 31, 2019

MANUSCRIPT ACCEPTED JULY 25, 2019

MANUSCRIPT HANDLED BY LINDSAY MCHENRY

Endnote:

¹Deposit item AM-19-126983, Supplemental tables and CIF. Deposit items are free to all readers and found on the MSA website, via the specific issue's Table of Contents (go to http://www.minsocam.org/MSA/AmMin/TOC/2019/Dec2019_data/Dec2019_data.html).